FOREWORD

This report was prepared by the Aerodynamics Branch of the X-20 (Dyna-Soar) Engineering Office, Aeronautical Systems Division, Wright-Patterson Air Force Base, Ohio, under Weapon System 620A. The work was accomplished by the author as partial fulfillment of the requirements for the degree of Doctor of Philosophy at The Ohio State University, Columbus, Ohio. The Ohio State University has granted permission to the USAF to publish and distribute the thesis as an ASD Technical Documentary Report. Only those changes necessary to make the thesis meet the requirements of an ASD Technical Documentary Report have been made.

The author is indebted to his adviser, Dr. Rudolph Edse of The Ohio State University for his assistance and guidance throughout the study. The cooperation and assistance of the following individuals of the Aeronautical Systems Division are gratefully acknowledged: Messrs Grover Alexander and Lawrence Hooks for the preparation of certain sections in the report; and Mr. Kenneth Cunningham and Miss Kathryn Beighle for the accomplishment of the manuscript.

ABSTRACT

The first successful recovery of man from space has been accomplished through the use of drag capsules. In a more advanced concept, aerodynamic lift is used during re-entry to provide range maneuverability so that a precise site can be selected and a horizontal landing capability can be provided. Maximum maneuverability may be achieved by modulating the hypersonic lift-to-drag ratio (L/D). In this study the lifting re-entry configuration was optimized to maximize hypersonic L/D within the heating, stability, and landing constraints. A flat bottom surface, clipped delta planform with a 0.32 taper ratio, dorsal delta fins, and elliptical (2:1) nose and leading edges were ascertained to produce maximum hypersonic L/D for the prescribed constraints. Eleven pertinent constraint equations were formulated, and numerical calculations of the complete aerodynamic characteristics and configurational geometry were determined. The IBM 7090 computer was used to solve the 11 constraint equations through an iteration technique and to perform the maximization process. Optimum configurational geometries were evaluated for three wing loadings at vehicle weights of 10,000 and 100,000 pounds. Results show that higher L/D values can be achieved with low aspect ratio, low wing loadings, and large scale vehicles. The complete geometry for one of the typical optimums is shown as an example.

PUBLICATION REVIEW

This technical documentary report has been reviewed and is approved.

FOR THE COMMANDER:

WILLIAM E. LAMAR
Chief, X-20 (Dyna-Soar) Engineering Office
Deputy for Engineering

TABLE OF CONTENTS

LIST OF ILLUSTRATIONS

LIST OF SYMBOLS

Symbol	Description	Units
A	area	ft^2
AR	aspect ratio = $\frac{b^2}{S}$	--
a	parameter = $\frac{1}{2}\frac{L}{D}\sin\phi$	--
b	span	ft
C	constant	--
c	root chord	ft
$\bar{c}$	mean aerodynamic chord	ft
$C_A = \frac{A}{q S}$	axial force coefficient	--
$C_Y = \frac{Y}{q S}$	side force coefficient	--
$C_N = \frac{N}{q S}$	normal force coefficient	--
$C_{\mathscr{l}} = \frac{\mathscr{L}}{qSb}$	rolling moment coefficient	--
$C_m = \frac{\mathscr{M}}{qS\bar{c}}$	pitching moment coefficient	--
$C_n = \frac{\mathscr{N}}{qSb}$	yawing moment coefficient	--
$C_L = \frac{L}{q S}$	lift coefficient	--
$C_D = \frac{D}{q S}$	drag coefficient	--
$C_p = \frac{P-P_\infty}{q_\infty}$	pressure coefficient	--
D	drag	lb
F	function defined in Equation (35) or function defined in Equation (72)	--
f	function	--
G	function defined in Equation (54)	--

LIST OF SYMBOLS (CONT'D)

Symbol	Description	Units
g	function defined in Equation (81) or acceleration of gravity	-- $ft/sec.^2$
$\underline{H}$	angular momentum vector	$slug\text{-}ft^2/sec.$
h	enthalpy	$ft^2/sec.^2$
h_F	fin height	ft
I	integral	--
$\underline{I}$	inertial dyadic in Equation (224), Appendix IV	$slug\text{-}ft^2$
$\underline{i}$	unit vector in x direction	--
$\underline{j}$	unit vector in y direction	--
$\underline{k}$	unit vector in z direction	--
k	Newtonian modifier, Equation (176), Appendix III	--
L	lift	lb
ℓ	leading edge length	--
M	Mach number	--
n	exponent in Equation (71)	--
$\underline{n}$	surface normal	--
m	taper ratio $= \frac{c_t}{c_r}$ or exponent	--
P	pressure	lb/ft^2
q	dynamic pressure	lb/ft^2
$\dot{q}$	heating rate	$BTU/(ft^2sec.)$
R	radius or range	ft
R_e	Reynolds number	--
S	reference planform area	ft^2

LIST OF SYMBOLS (CONT'D)

Symbol	Description	Units
s	arc length	ft
T	torque or temperature	ft lb °R
t	time	sec.
V	flight velocity	ft/sec.
$V_c = g R_E$	circular velocity = 25,930	ft/sec.
W	weight	lb
x y z	orthogonal coordinate system in body axes	ft ft ft
Greek		
α	angle of attack = $\tan^{-1} \frac{w}{u}$	radians
β	angle of sideslip = $\sin^{-1} \frac{v}{\lvert \underline{V} \rvert}$	radians
γ	specific heat ratio = 1.4 or flight path angle	-- radians
Δ	incremental difference	--
δ	flow deflection angle	radians
ϵ	emissivity	--
ζ	damping ratio	--
θ	pitch angle	radians
Λ	sweep angle	radians
λ	Lagrangian multiplier or fin toe in angle (Figure 3)	-- radians
μ	dynamic viscosity	lb sec./ft^2
ν	kinematic viscosity	ft^2/sec.

LIST OF SYMBOLS (CONT'D)

Symbol	Description	Units
ρ	density	$slug/ft^3$
σ	Stephan-Boltzmann constant $= 0.481 \times 10^{-12}$	$\frac{BTU}{(ft^2\ sec.\ {}^\circ R^4)}$
ϕ	roll angle	radians
ψ	heading angle	radians
ω	angular velocity	radians/sec.

Subscripts

c.g.	center of gravity
e	effective angle
F	fin
FLE	fin leading edge
i	initial value
LE	leading edge
LS	lower surface
max	maximum value
N	nose
opt	optimum value, at $(L/D)_{max}$
s	stagnation condition
sh	shoulder value
∞	free stream condition
δ	condition at outer edge of boundary layer

SECTION 1

INTRODUCTION

The first successful recovery of objects from space has been achieved by means of ballistic devices. The entry angles for such devices are steep, and since the associated re-entry duration is short, heat-sink or ablative thermal-protective systems have been used. Large decelerations are associated with steep re-entry angles, which necessitates shallow re-entry angles to recover a manned vehicle from space. The duration of heating increases with this mode of entry, however, and low values of the ballistic coefficient $(\frac{W}{C_D A})$ are required to minimize the heat load. Again, heat-sink or ablation schemes may be used successfully. The pure drag re-entry, as represented by the NASA Mercury capsule, offers the simplest and most efficient method of achieving manned re-entry from space. The drag capsule designed to possess a low ballistic coefficient, protected efficiently from the severe heat pulse of a few minutes duration by an ablative coating, enters with a nominal deceleration of about 8 g's, which is within man's toleration limits. A soft landing over water is accomplished by deploying a drag chute after the dynamic pressure subsides. The landing site is restricted to lie in the orbital plane since no ability to produce lateral range exists, and once the retro rocket is fired to initiate re-entry, no vernier control or modulation of longitudinal range is available. Selection of landing site is possible at the expense of waiting several orbits until the earth rotates within the orbital plane. The additional propulsive weight required to produce sufficient transverse impulse, which provides a large rotation of the orbital plane, is impractical with present day rocketry. In short, the drag mode provides for a safe re-entry with little choice of precise site selection.

Since the use of aerodynamic drag has proved to be a much more efficient means of decelerating re-entry vehicles than propulsion, the investigation of the use of aerodynamic lift to achieve lateral maneuverability follows naturally. Lifting re-entry configurations also offer the potential of providing horizontal landing, which would furnish better operational capability because large recovery task forces and the perils of parachute landings in water would be eliminated. Lifting configurations are more complex because of the additional flight-control system, variable stability, higher required performance, and longer flight duration in the sensible atmosphere. The duration of the lifting re-entry heating pulse is measured in hours instead of minutes as in the drag mode; therefore, ablation techniques are impractical. Instead, the radiation cooling concept is used. The surface is permitted to reach a sufficiently high temperature so that the radiation heat efflux balances the convective heat influx and an energy equilibrium occurs. The resulting high temperatures require heavy outer panels to protect the interior structure. Thus, the lifting re-entry vehicle incurs a greater weight penalty than the drag capsule but achieves the greater performance of lateral maneuverability, range modulation, and horizontal landing. In short, for missions requiring lateral maneuverability and precise site selection as well as horizontal landing, the lifting mode is desirable.

Manuscript released by author on 31 December 1962 for publication as an ASD Technical Documentary Report.

Because of the greater weight of the lifting device, the aircraft designer is forced to optimize the configuration. The purpose of this investigation is to perform the optimization of lifting re-entry configurations to achieve maximum performance for the minimum weight.

Before attempting the design of the vehicle, we must further delineate the design objectives:

1. Achieve successful manned re-entry from circular speeds

2. Provide large lateral maneuverability and longitudinal range modulation

3. Provide satisfactory landing characteristics

4. Protect the vehicle from the aerodynamic heating

5. Provide the vehicle with adequate stability to produce satisfactory handling qualities.

SECTION 2

CONSTRAINTS

With the establishment of the objectives and requirements, the formulation of the problem and the conversion of the physical situation into the mathematical follow. The objectives stated in the Introduction will now be separately converted into definite mathematical expressions.

1. Achieve successful manned re-entry from circular speeds

Circular speed is 25,930 feet per second. For lifting re-entry, the following equilibrium glide expression applies (Equation 136, Appendix I):

$$\frac{1}{2} \rho V^2 = \frac{W}{SC_L} \left(1 - \frac{V^2}{V_c^2} \right) \tag{1}$$

A subtle implication in this statement is that man and vehicle have been inserted into a near-earth circular orbit by an existing or programmed booster. Since rocket boosters are inefficient propulsion devices (approximately 100 pounds of propulsion is required to place 1 pound into orbit) and permit small limited payloads, the re-entry vehicle is weight-limited. Hence, the specified weight of the re-entry vehicle is constrained. Therefore,

$$W = \text{fixed values.} \tag{2}$$

2. Provide large maneuverability and longitudinal range modulation

As pointed out in Appendix I, maximum lateral and longitudinal range may be achieved by optimizing the hypersonic L/D (lift-to-drag ratio) of the re-entry spacecraft. Thus, the hypersonic L/D should be maximized within the specified constraints. The hypersonic aerodynamic characteristics for a generalized configuration are expressed in Equations (190) through (216), Appendix III.

3. Provide satisfactory landing characteristics

For a successful landing, the sinking speed, horizontal velocity, and attitude must be limited to reasonably low values at touchdown. Appendix V shows these minimum acceptable subsonic vehicle characteristics, which permit a satisfactory landing to be expressed as follows:

$$\frac{W}{S\,AR} = 50 \text{ pounds per square foot} \tag{3}$$

4. Protect the vehicle from aerodynamic heating

The most efficient and practical technique for protecting a glide vehicle from aerodynamic heating is the radiation cooling concept described in Appendix II. The vehicle must be constructed and flown so as not to exceed the allowable material temperatures by means of unacceptable attitude, performance, or geometry. Thus, the maximum vehicle temperature is limited. Four critical

locations affecting geometry will be specified and may be computed from Equations (155), (169), (170), and (172) of Appendix II. Thus, nose, wing and fin leading edges, and lower surface maximum temperature are constrained. Therefore,

$$T_N = \text{fixed value} \tag{4}$$

$$T_{LE} = \text{fixed value} \tag{5}$$

$$T_{FLE} = \text{fixed value} \tag{6}$$

$$T_{LS} = \text{fixed value.} \tag{7}$$

5. Provide the vehicle with adequate stability to produce satisfactory handling qualities

Pilot-rated simulator studies have indicated that the most desirable handling qualities are obtained when the short-period mode of the rigid body has a frequency of 0.7 cycle per second and a damping ratio of 0.7 (Appendix IV). In hypersonic flight negligible aerodynamic damping occurs, which necessitates changing the handling quality criteria. Therefore, very low frequencies are required for the pilot to damp-out quickly oscillations by "out of phase" control modulation. Zero frequency may be obtained by imposing neutral aerodynamic stability or

$$C_{\ell_\beta} = 0 \tag{8}$$

$$C_{m_\alpha} = 0 \tag{9}$$

$$C_{n_\beta} = 0 \tag{10}$$

as M approaches infinity.

Appendix V shows that a fin size of 10 percent of the reference planform area is required to provide satisfactory subsonic directional stability. Hence,

$$\frac{S_F}{S} = 0.1 \ . \tag{11}$$

The problem becomes one of optimizing the geometry of the vehicle to maximize the hypersonic L/D when the specified 11 constraint equations are used. A solution will be obtained in the following sections by first determining the component geometry that maximizes hypersonic L/D and then combining these components into a composite configuration and optimizing the complete geometry to satisfy the 11 constraint equations.

SECTION 3

OPTIMIZATION OF COMPONENTS

Since an optimization of the vehicle as proposed is so complex, we shall pursue the problem by analyzing configuration components to determine maximum performance, then by combining the pieces, and by checking for compatibility.

We shall attempt to maximize hypersonic performance characteristics within the constraints previously outlined in the following order:

1. Lower surface
2. Planform
3. Vertical fin
4. Nose and leading edge geometry.

With this accomplished, the entire composite configuration will be optimized later in Section 4.

3-A. Lower Surface

The objective of this section is to determine the shape of the exposed lower surface to produce the maximum hypersonic L/D. A coordinate system is established in the conventional wind axes system (Figure 1).

To assist us in providing directional stability, we establish a plane of symmetry. The plane that contains the x and z axes is chosen as the plane of symmetry for which a mirror image relationship exists between surfaces on alternate sides of the x-z plane.

The equation for a surface is

$$z - f(x, y) = 0 . \tag{12}$$

The equation for the outward normal to the surface is

$$\underline{n} = \frac{\nabla (z - f)}{|\nabla (z - f)|} . \tag{13}$$

Expansion of Equation (13) produces the following relationship:

$$\underline{n} = \frac{-i \frac{\partial z}{\partial x} - \underline{j} \frac{\partial z}{\partial y} + \underline{k}}{\sqrt{1 + \left(\frac{\partial z}{\partial x}\right)^2 + \left(\frac{\partial z}{\partial y}\right)^2}} . \tag{14}$$

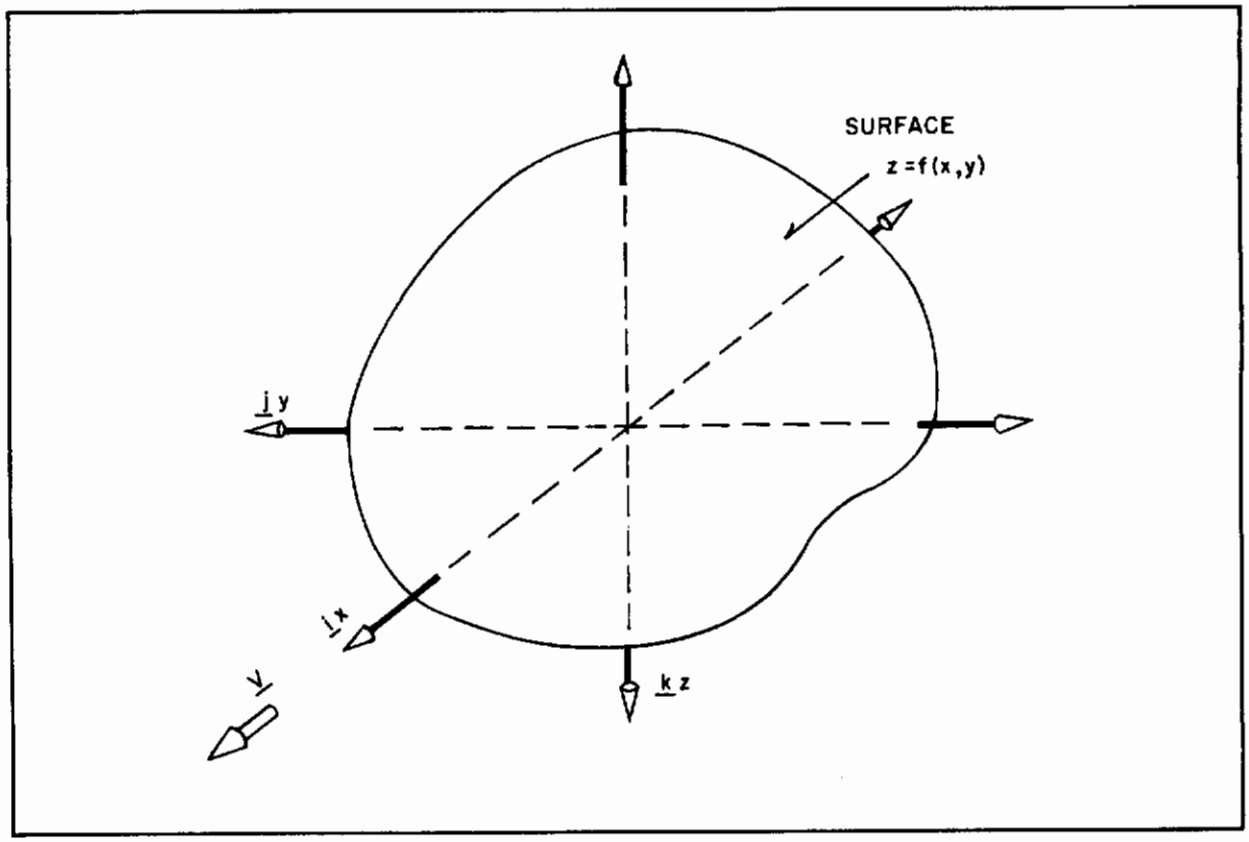

Figure 1. Generalized Surface in Wind Axes Coordinate System

The elemental area is expressed as follows:

$$dA = \sqrt{1 + \left(\frac{\partial z}{\partial x}\right)^2 + \left(\frac{\partial z}{\partial y}\right)^2}\ dx\ dy\ . \tag{15}$$

As indicated in Appendix III, only the continuum regime requires investigation so that modified Newtonian flow may be used in ascertaining the pressure on the surface in hypersonic flight as represented by the following equation:

$$C_p = k \cos^2 \theta \tag{16}$$

where θ is the angle between the surface normal and the velocity vector, or

$$\frac{\underline{V}}{|\underline{V}|} \cdot \underline{n} = \cos \theta\ . \tag{17}$$

Therefore, by use of Equation (14) and since

$$\underline{V} = \underline{i}\ |\underline{V}| \tag{18}$$

then Equation (17) becomes

$$\cos^2\theta = \frac{\left(\frac{\partial z}{\partial x}\right)^2}{1+\left(\frac{\partial z}{\partial x}\right)^2+\left(\frac{\partial z}{\partial y}\right)^2} \tag{19}$$

The lift and drag are determined in the following usual manner:

$$L = q \iint_A C_p \, (\underline{n} \cdot \underline{k}) \, dA \quad . \tag{20}$$

When Equations (14), (15), (16), and (19) are used,

$$L = q \iint_A \frac{k \left(\frac{\partial z}{\partial x}\right)^2 dx \, dy}{1+\left(\frac{\partial z}{\partial x}\right)^2+\left(\frac{\partial z}{\partial y}\right)^2} \tag{21}$$

and

$$D = q \iint_A C_p \, (\underline{n} \cdot \underline{i}) \, dA \quad ; \tag{22}$$

similarly

$$D = q \iint_A \frac{k \left(-\frac{\partial z}{\partial x}\right)^3 dx \, dy}{1+\left(\frac{\partial z}{\partial x}\right)^2+\left(\frac{\partial z}{\partial y}\right)^2} \tag{23}$$

The surface z(x,y) that maximizes L/D will be determined by using the calculus of variations.

L/D is maximized by using a Lagrangian multiplier and maximizing the lift for a fixed drag.

$$I_1 = L + \lambda_1 D \tag{24}$$

or rewriting

$$I_1 = q \iint_A F \, dx \, dy = \text{extremal} \quad ! \tag{25}$$

where

$$F = \frac{k \left(\frac{\partial z}{\partial x}\right)^2 \left(1 - \lambda_1 \frac{\partial z}{\partial x}\right)}{1+\left(\frac{\partial z}{\partial x}\right)^2+\left(\frac{\partial z}{\partial y}\right)^2} \tag{26}$$

and q = constant for given flight conditions.

Euler's equation for a double integral is as follows (Reference 1):

$$\frac{\partial}{\partial x} F_{z_x} + \frac{\partial}{\partial y} F_{z_y} = F_z \tag{27}$$

with boundary conditions for free ends

$$F_{z_x} \frac{dy}{dx} = F_{z_y} \quad \text{on the boundary of A.} \tag{28}$$

Since

$$F = F(z_x, z_y) \tag{29}$$

then

$$F_z = 0 \tag{30}$$

Thus an obvious particular solution of Equations (27) and (30) is that

$$F_{z_x} = C_1 \; ; \tag{31}$$

hence, from Equation (27)

$$F_{z_y} = C_2 \tag{32}$$

From the boundary condition, Equation (28),

$$C_1 \frac{dy}{dx} = C_2 \quad \text{on A boundary.} \tag{33}$$

Since $\frac{dy}{dx}$ is arbitrary and not necessarily constant, the C_1 and C_2 must be identically zero. Proceeding with the solution by expanding Equation (32) gives

$$F_{z_y} = \frac{-2kz_x^2 (1-\lambda_1 z_x) z_y}{(1 + z_x^2 + z_y^2)^2} = C_2 = 0. \tag{34}$$

Five possible solutions satisfy the Equation (34)

$$z_x = 0, \frac{1}{\lambda_1}, \infty,$$

$$z_y = 0, \infty.$$

However, F = 0, which corresponds to a minimum, for all values except for $z_y = 0$.

Since $F_{z_x} = C_1 = 0$ (Equation 31) and $z_y = 0$, then by integration of Equation (31) which is now a total differential equation

$$F = C_3 = \frac{k z_x^2 (1 - \lambda_1 z_x)}{1 + z_x^2} \quad . \tag{35}$$

Equation (35) is a cubic equation in z_x with constant coefficients. Thus,

$$z_x = C_4 \quad , \tag{36}$$

and since $z_y = 0$,

$$z = C_4 x + C_5 \quad . \tag{37}$$

Therefore, the surface that produces a relative maximum hypersonic L/D is a plane parallel to the y-axis at an attitude of α such that $C_4 = -\tan \alpha$.

This particular solution remains to be proved as the one desired. The solution was obtained by inspection of Equation (27), i.e., $F_{z_x} = C_1$, Equation (31). It followed that $z_y = 0$ for this situation. Therefore, a maximum extremal for the following equation was obtained:

$$I_0 = \iint_A \frac{k z_x^2 (1 - \lambda_1 z_x) \, dx \, dy}{1 + z_x^2} \quad . \tag{38}$$

The more general equation for which a solution is desired is the following:

$$I_1 = \iint_A \frac{k z_x^2 (1 - \lambda_1 z_x) \, dx \, dy}{1 + z_x^2 + z_y^2} \tag{39}$$

But z_y is real in the physical problem; therefore, $z_y^2 \geq 0$. Since z_y^2 appears in the denominator of Equation (39), it is apparent that

$$I_1 < I_0 \quad \text{for} \quad z_y \neq 0 \tag{40}$$

and

$$I_1 = I_0 \quad \text{for} \quad z_y = 0 \quad . \tag{41}$$

Therefore since the maximum value of I_1 is desired, and the solution of I_0 produces the maximum extremal of I_1, the solution obtained by inspection ($F_{z_x} = C_1$, Equation 31) is the desired solution.

3-B. Planform

By using the results of the optimized surface (i.e. flat bottom surface), we shall optimize the planform geometry. Because of the heating constraint, the edges of the planform must possess a finite radius to maintain specified nose and leading edge allowable temperatures (see Equations 169 and 170 of Appendix II). These radii should be as small as the heating constraint permits to produce minimum drag. The expression for the nose and leading edge aerodynamic coefficients (from Appendix III) is as follows:

$$C_{D_o} = \frac{k \pi R_N^2}{2S} + \frac{8k}{3S} \int_0^C \left(\frac{dy}{dx}\right) R_{LE} \cos^2 \Lambda \, dx \tag{42}$$

and

$$C_{L_o} \cong 0 .$$

The contribution to the total lift coefficient is negligible for the situation in which the nose and leading edge areas are small as compared to the total planform area. Since the nose and leading edges are temperature-limited (see constraint Equations 4 and 5),

$$R_{LE} = R_o \cos^2 \Lambda \tag{43}$$

where R_o = constant for specified flight conditions and temperature limit. From the planform geometry

$$\cos^2 \Lambda = \frac{\cot^2 \Lambda}{1 + \cot^2 \Lambda} \cong \left(\frac{dy}{dx}\right)^2 \text{ for large } \Lambda \text{ values.} \tag{44}$$

Thus when Equations (42), (43), and (44) are combined,

$$C_{D_o} = \frac{k \pi R_N^2}{2S} + \frac{8k R_o}{3S} \int_0^C \left(\frac{dy}{dx}\right)^5 dx \tag{45}$$

where

$$S = 2 \int_0^C y \, dx \tag{46}$$

The L/D of the configuration can be maximized by minimizing C_{D_o} for prescribed planform surface area, S, and fixed nose and leading edge temperature. The integral, which must be rendered an extremal, is as follows:

$$I_2 = C_{D_o} + \lambda_2 S = \int_0^C G \, dx \tag{47}$$

where from Equations (45) and (46)

$$G = \left(\frac{dy}{dx}\right)^5 + \lambda_2 y . \tag{48}$$

The end conditions that pertain are as follows:

at the nose,

$$\left.\begin{aligned} x &= c \\ y &= 0 \end{aligned}\right\} \text{ fixed end}$$

at the trailing edge,

$$\left.\begin{aligned} x &= 0 \\ \frac{\partial G}{\partial y'} &= 0 \end{aligned}\right\} \text{ free end.}$$

Euler's equation for $G = G(x,y,y')$ is

$$\frac{d}{dx} G_{y'} = G_y \tag{49}$$

or when Equation (48) is used,

$$\frac{d}{dx} (5y'^4) = \lambda_2 \ . \tag{50}$$

Integrating with respect to x and using the free-end boundary condition ($G_{y'} = 0$ at $x = 0$) gives

$$\frac{dy}{dx} = (0.2\, \lambda_2\, x)^{\frac{1}{4}} \ . \tag{51}$$

Integrating again with respect to x and using the fixed-end boundary condition ($y = 0$, $x = c$) produces the following:

$$y = -\frac{4}{5} c^{\frac{5}{4}} (0.2\, \lambda_2)^{\frac{1}{4}} \left[1 - \left(\frac{x}{c}\right)^{\frac{5}{4}}\right] \tag{52}$$

λ_2 may now be determined from the condition that S must be constant when Equation (46) is integrated. Thus the planform for minimum C_{D_o} is

$$y = \frac{0.9S}{c} \left[1 - \left(\frac{x}{c}\right)^{\frac{5}{4}}\right] \ . \tag{53}$$

However, $y = \frac{b}{2}$ at $x = 0$ and $S = \frac{bc}{1.8}$. Hence,

$$\left(1 - \frac{2y}{b}\right) = \left(\frac{x}{c}\right)^{\frac{5}{4}} \tag{54}$$

Thus, for fixed area and a constant-temperature leading edge, the minimum drag planform is a 5/4 power curve. The resulting configuration is not extremely practical from a fabrication standpoint since both a variable leading-edge radius and variable sweep are involved. In addition, the combination of fin and wing together at angle of attack must be considered. Because of the incompleteness of this analysis, the 5/4 power curve should be used only as a guide to enable the optimization of the composite

configuration. For example, a simple delta may be used to approximate the 5/4 power curve and does not require variable leading-edge radii or sweep (note Figure 2).

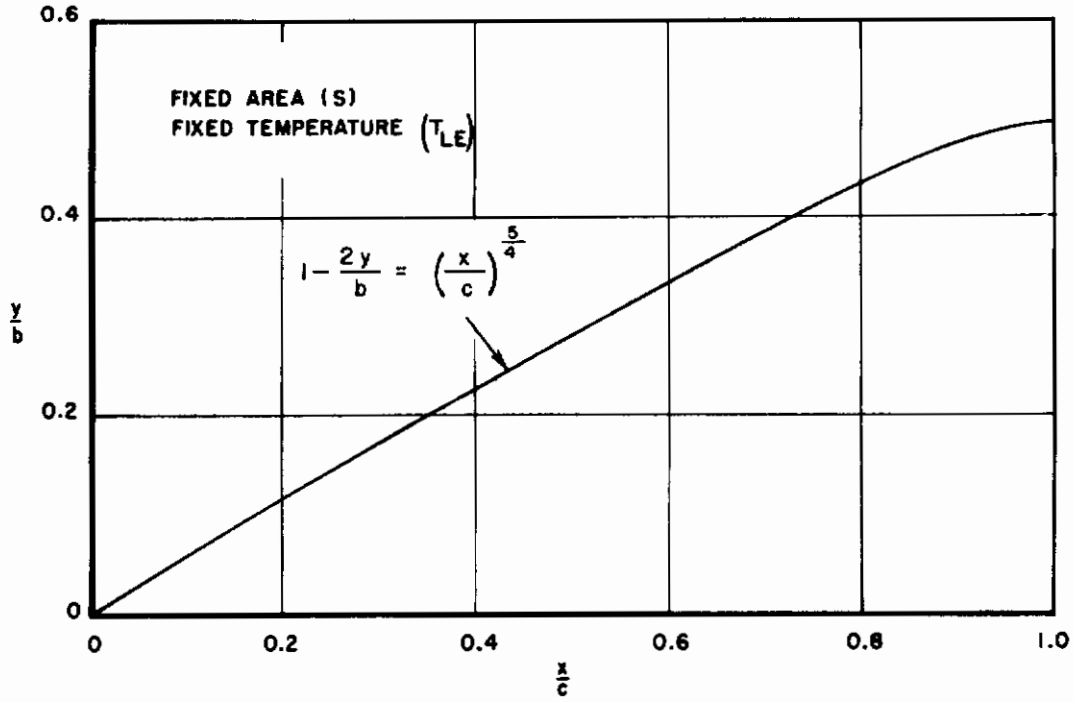

Figure 2. Geometry of Minimum Drag Planform

3-C. Taper Ratio

When the stability constraint is imposed, it becomes apparent the profile area aft of the center of gravity (c.g.) is required to provide directional stability at all speeds. Conventionally, vertical fins in the most aft position have been used to provide this stability. A ventral fin would most efficiently provide the desired stability; however, the heating is so severe that the dorsal position is the only presently acceptable location. Dorsals also provide lower drag than a ventral (for the same material-temperature limit) because of the greater effective sweep when operating at angle of attack greater than zero. Since the upper surface is shielded hypersonically, two dorsal fins located outboard in the most aft position are required. As previously shown, the planform of fixed area, temperature, and chord that presents the minimum leading edge drag is close to a delta shape (Figure 2). For this reason the vertical fin will be configured in this optimum delta shape. Thus the optimum configuration possesses a flat bottom (Section 3-A), a delta shaped planform (Section 3-B), and two delta dorsal vertical outboard fins. The vertical fins can be attached effectively, however, by clipping the planform delta as shown in Figure 3. Note the root chord of length c, taper ratio m, wing sweep Λ, and fin leading edge sweep Λ_F. This geometry will be optimized for maximum L/D, by imposing the constraints established in Section 2.

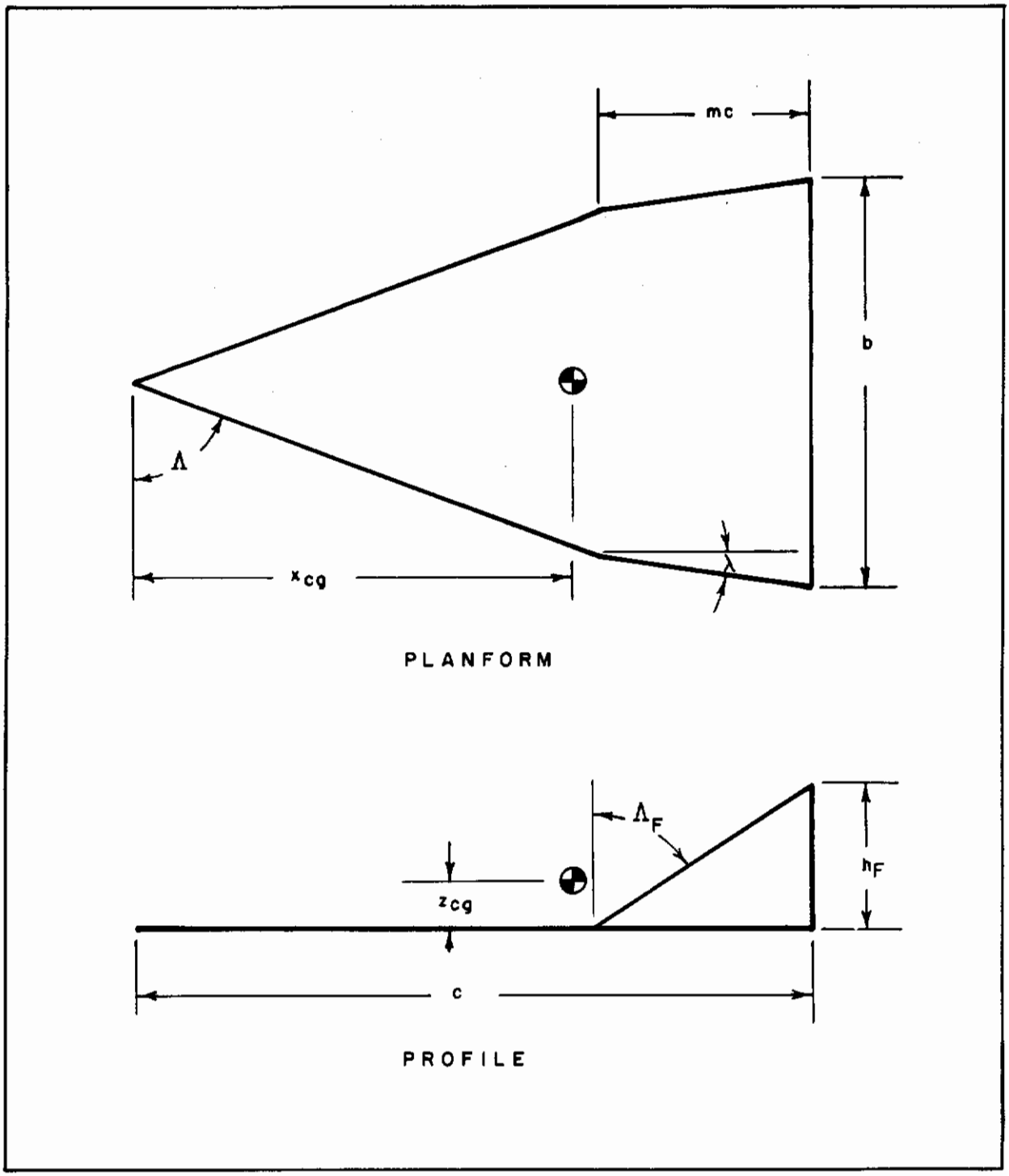

Figure 3. Geometry Model for Optimizing Taper Ratio

The axial force coefficient of all components for the described configuration is as follows (see Appendix III):

$$C_A = \frac{\pi k R_N^2}{8S}(1+\cos\alpha)^2 + \frac{k R_{LE} b}{3S}(\cos\Lambda_e + \cos\Lambda\cos\alpha)^2$$

$$+ 2k\frac{S_F}{S}\lambda^3\cos^2\alpha + \frac{8k R_F h_F}{3S}\cos^2(\Lambda_F+\alpha)$$

$$+ \frac{8}{3}\frac{S_w}{S}\frac{0.45\cos\alpha + 4.65\left(\frac{V_\infty}{10,000}\right)\sin\alpha\cos^{2.2}\alpha}{\left(\frac{V_\infty c}{\nu_\infty}\right)^{0.5}}\left(\frac{1-m^{1.5}}{1-m^2}\right). \qquad (55)$$

From the heating equations of Appendix II

$$R_N = \frac{W}{SC_L}\left(\frac{8.025}{\dot{q}_N}\right)^2 \qquad (56)$$

$$R_{LE} = \frac{W}{SC_L}\left(\frac{5.675}{\dot{q}_{LE}}\right)^2\cos^2\Lambda_e \qquad (57)$$

where

$$\cos^2\Lambda_e = 1-\sin^2\Lambda\cos^2\alpha \quad \text{for wing leading edge}$$

$$\cos^2\Lambda_e = \cos^2(\Lambda_F+\alpha) \quad \text{for fin leading edge}.$$

The critical design point for heating is

$$V_\infty = 21{,}170 \text{ feet per second (Appendix II).}$$

When the equilibrium glide equation (Appendix I) is used, the Reynolds number may be ascertained.

$$\frac{V_\infty c}{\nu_\infty} \quad \frac{2W c}{S C_L \mu_\infty V_\infty}\left(1-\frac{V_\infty^2}{V_c^2}\right). \qquad (58)$$

At critical heating and for $\mu_\infty \approx 3 \times 10^{-7}$ lb-sec./ft^2

$$\frac{V_\infty c}{\nu_\infty} = \frac{105 W c}{S C_L}. \qquad (59)$$

From the geometry of Figure 3, the following quantities may be obtained (for small λ values):

$$\frac{b}{c} = \frac{AR}{2}(1+m), \qquad (60)$$

where

$$AR = \frac{b^2}{S}$$

$$\frac{h_F}{b} = \left(\frac{1+m}{m}\right)\frac{S_F}{S} \tag{61}$$

and

$$\cot \Lambda = \frac{AR}{4}\left(\frac{1+m}{1-m}\right) \tag{62}$$

$$\cot \Lambda_F = \frac{AR}{2}\,\frac{S_F}{S}\left(\frac{1+m}{m}\right)^2 . \tag{63}$$

Substitution of Equations (56), (57), (59), (60), and (61) into Equation (55) results in the following:

$$\begin{aligned} C_A = {} & \frac{\pi k (1+\cos\alpha)^2}{8W C_L^2}\left(\frac{W}{S}\right)^3\left(\frac{8.025}{\dot{q}_N}\right)^4 \\ & + \frac{kb}{3W C_L}\left(\frac{W}{S}\right)^2\left(\frac{5.675}{\dot{q}_{LE}}\right)^2\left[\cos^2\Lambda_e(\cos\Lambda_e+\cos\Lambda\cos\alpha)^2\right. \\ & \left. + \frac{8S_F}{S}\left(\frac{1+m}{m}\right)\cos^4(\Lambda_F+\alpha)\right] + 2k\,\frac{S_F}{S}\,\lambda^3\cos^2\alpha \\ & + \frac{\dot{8}}{3}\,\frac{S_W}{S}\left(\frac{b C_L}{210W}\right)^{0.5}(0.45\cos\alpha + 9.84\sin\alpha\cos^{2.2}\alpha)\,\frac{(1+m)^{0.5}(1-m^{1.5})}{(1-m^2)} . \end{aligned} \tag{64}$$

When Equation (64) is written in functional form with the aid of Equations (62) and (63),

$$\begin{aligned} C_A = {} & C_{A_{NOSE}}\left(W, \frac{W}{S}, \dot{q}_N, \alpha\right) \\ & + C_{A_{LE}}\left(b, W, \frac{W}{S}, \dot{q}_{LE}, \frac{S_F}{S}, \alpha, m\right) \\ & + C_{A_{FIN}}\left(\frac{S_F}{S}, \lambda, \alpha\right) \\ & + C_f\left(\frac{S_W}{S}, b, W, \alpha, m\right) . \end{aligned} \tag{65}$$

However, from the constraints imposed as given in Section 2

		constraint equation
W	$=$ constant	(2)
b	$= \frac{W^{0.5}}{\sqrt{50}} =$ constant	(3)
$\dot{q}_N$	$=$ constant	(4)
$\dot{q}_{LE}$	$=$ constant	(5,6)
$\dot{q}_{LS}$	$= 2.26 \left(\frac{W}{S}\right)^{0.8} =$ constant	(7)
$\frac{S_F}{S}$	$= 0.1$	(11)

For $\frac{S_W}{S} = 2$, $\alpha = \alpha_{opt}$ and λ determined from constraint Equation (9) then Equation (65) becomes $C_A = C_A(m)$. To maximize L/D, one should optimize the taper ratio (m) to minimize C_A. Only the second and fourth terms (leading edge and skin friction terms) of Equations (64) and (65) depend upon m. However, the skin friction expression depends only mildly upon m as follows:

m	$(1+m)^{0.5} \quad \frac{1-m^{1.5}}{1-m^2}$
0	1.000
0.2	1.039
0.4	1.052
0.6	1.058
0.8	1.060
1.0	1.061

Therefore for constants W, b, and α, the laminar skin friction coefficient is virtually independent of taper ratio (only ±3 percent variation). Hence the optimum taper ratio must be determined from the condition for minimum leading edge drag.

The leading edge drag component of Equation (64) may be written as

$$\left(\frac{3S}{k\,b\,R_0}\right) C_{D_{LE}} = \cos^2\Lambda_e \left(\cos\Lambda_e + \cos\Lambda\cos\alpha\right)^2 + \frac{8S_F}{S}\left(\frac{1+m}{m}\right)\cos^4\left(\Lambda_F + \alpha\right) \qquad (66)$$

where

$$R_o = \frac{W}{SC_L} \left(\frac{5.675}{q_{LE}} \right)^2 . \tag{67}$$

When the geometric relationships (Equations 62 and 63) are used, Equation (66) may be solved for various values of m, $\frac{S_F}{S} = 0.1$, and for fixed values of AR and α. In the region of interest ($0.5 < AR < 2$ and $10° < \alpha < 25°$), numerical calculations show that a taper ratio between 0.30 and 0.35 produces minimum total leading edge drag (Figure 4). Therefore, an average value of 0.32 for optimum taper ratio was selected. Since the c.g. must be located near the area centroid of the lower surface (about 0.35 c from the trailing edge) to satisfy the pitch stability constraint (Equation 9), the optimum taper ratio of 0.32 advantageously places the entire vertical fin aft of the c.g.

For the configurations to be investigated herein, a taper ratio of 0.32 was adopted. However, note that for values of $\frac{S_F}{S}$, AR, and α, which are much different than those stated above, sizable differences in optimum taper ratio values will result.

3-D. Nose and Leading Edge

The flight corridor of re-entry vehicles is limited by its ability to absorb or reject the re-entry heat load. The heat pulse applied to a ballistic vehicle during re-entry is of such short duration that cooling by ablation allows the vehicle to survive. Because of long re-entry times, however, the only presently practical way to cool lifting vehicles is by radiating their heat loads to space. The long re-entry time and small heat capacity of a lifting vehicle's skin results in equilibrium between heat convected to and heat radiated away from the surface.

The objective of this section is to determine the detailed shape of the nose and leading edge that will minimize the peak temperature. When the peak temperature is minimized, smaller radii configurations may be employed, which result in lower total drag.

As shown in Appendix II, the highest heating occurs at the stagnation region in laminar flow at a velocity of 21,170 feet per second during glide re-entry. Consider the total heating rate into a surface in radiation equilibrium flying at this peak heating point

$$\dot{Q} = \int \dot{q} \, dA = \epsilon \sigma \int T^4 \, dA \tag{68}$$

where constant emissivity has been assumed. An average temperature may be defined as follows:

$$T_{avg}^4 \int dA = \int T^4 \, dA \tag{69}$$

or

$$\frac{1}{A} \int \left(\frac{T}{T_{avg}} \right)^4 dA = 1. \tag{70}$$

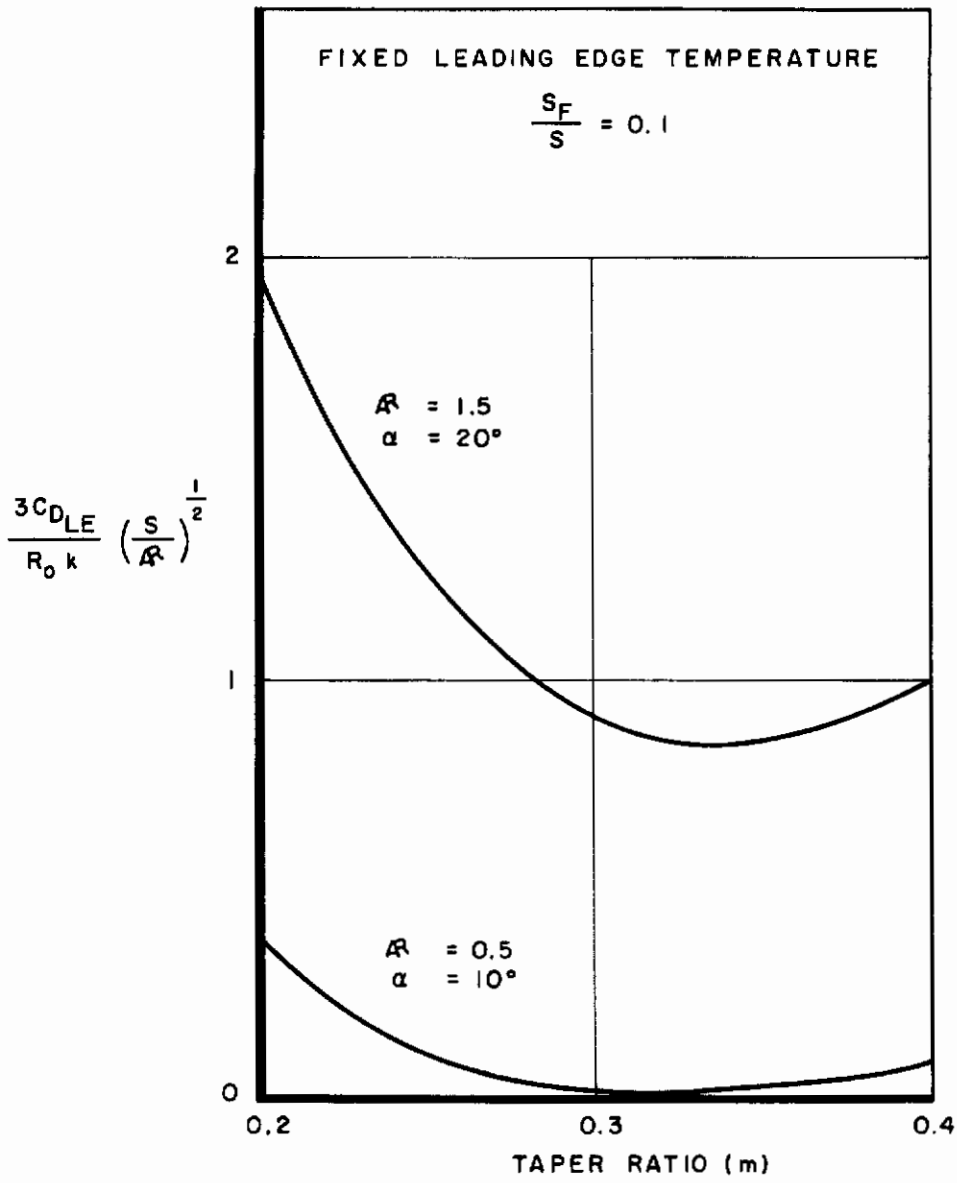

Figure 4. Wing and Fin Leading-Edge Drag Versus Taper Ratio

If a region of A exists for which $T < T_{avg}$, Equation (3) shows that another region must exist for which $T > T_{avg}$. Thus, the surface characterized by A, $\dot{Q}$, and ϵ, which has a constant surface temperature $T \equiv T_{avg}$, has the minimum peak temperature of all surfaces characterized by A, $\dot{Q}$, and ϵ. Since q is related monotonically to T, a constant $T = T_{avg}$ implies a constant $\dot{q} = \dot{q}_{avg}$. Therefore, for a surface characterized by A, $\dot{Q}$, and ϵ, which is maintaining thermal equilibrium by radiation, the minimum peak temperature will occur when the local heating rate on A is a constant $\dot{q} = \epsilon\sigma T_{avg}^4$. Thus, the problem of finding the optimum nose and leading edge geometry is reduced to that of finding a surface of constant heating rate.

Lees (Reference 2) describes the laminar convective heat-transfer rate near the stagnation point of a blunt body in hypersonic flight by

$$\frac{\dot{q}}{\dot{q}_s} = \frac{F(s)}{2^{\frac{n}{2}} \left[\frac{1}{R_s} \left(\frac{R d V_\delta}{V_\infty \, ds} \right)_s \right]^{\frac{1}{2}}} \tag{71}$$

where

$$F(s) = \frac{\frac{P}{P_s} \; \frac{\omega_\delta}{\omega_s} \; \frac{V_\delta}{V_\infty} \; y^n}{\left[2 \int_0^s \frac{P}{P_s} \; \frac{\omega_\delta}{\omega_s} \; \frac{V_\delta}{V_\infty} \; y^{2n} \, ds \right]^{\frac{1}{2}}} \tag{72}$$

where n = 0 for a planar body (leading edge) and n = 1 for a body of revolution (nose).

The static pressure ratio will be represented by the Newtonian flow approximation

$$\frac{P}{P_s} = \cos^2 \theta \tag{73}$$

with θ as the angle between the surface normal and the velocity vector. Measurements by M. O. Creager (Reference 3) and others show that the total pressure is nearly constant along inviscid streamlines following a blunt body contour. When this is assumed, the local velocity at the outer edge of the boundary layer may be related to the local pressure by the following isentropic relationship:

$$\left(\frac{V_\delta}{V_\infty} \right)^2 = \frac{2 h_s}{V_\infty^2} \left[1 - \left(\frac{P}{P_s} \right)^{\frac{\gamma - 1}{\gamma}} \right] . \tag{74}$$

For hypersonic velocities:

$$\frac{2 h_s}{V^2} \approx 1 . \tag{75}$$

Substituting Equations (73) and (75) in Equation (74) gives

$$\frac{V_\delta}{V_\infty} = \left[1 - \cos^{2\beta^2} \theta \right]^{\frac{1}{2}} \tag{76}$$

where

$$\beta^2 = \frac{\gamma - 1}{\gamma} .$$

The velocity gradient may now be determined

$$\frac{dV}{ds} = V_\infty \beta^2 \left[1-\cos^2 2\beta^2 \theta\right]^{-\frac{1}{2}} \cos^2 2\beta^2 \theta \tan\theta \frac{d\theta}{ds} \tag{77}$$

The value of the velocity gradient at the stagnation point is required for Lees' heating rate equation.

$$\left(\frac{R}{V_\infty}\frac{dV\delta}{ds}\right)_s = \left[\frac{\beta^2 \tan\theta}{\left(1-\cos^2 2\beta^2\theta\right)^{\frac{1}{2}}}\right]_{\theta\to 0} = \beta \tag{78}$$

where

$$\frac{ds}{d\theta} = R. \tag{79}$$

When Equations (72), (73), (76), and (78) are used in Equation (71), the heating rate distribution may be obtained for an arbitrary body. Following Lees (Reference 2), the assumption is made that $\frac{\omega\,\delta}{\omega_s} = 1$ in hypersonic flight.

$$\frac{\dot{q}}{\dot{q}_s} = \frac{\cos^2\theta \left(1-\cos^2 2\beta^2\theta\right)^{\frac{1}{2}} \left(\frac{y}{R_s}\right)^n}{2^{\frac{n+1}{2}} \beta^{\frac{1}{2}} \left[\int_0^{\frac{s}{R_s}} \cos^2\theta \left(1-\cos^2 2\beta^2\theta\right)^{\frac{1}{2}} \left(\frac{y}{R_s}\right)^{2n} d\left(\frac{s}{R_s}\right)\right]^{\frac{1}{2}}} . \tag{80}$$

Wagner, Pine, and Henderson (Reference 4) have shown experimentally that Lees' equation holds well for a series of blunt-nosed bodies with noncircular cross-sections.

Since R_s appears only as a scaling factor in Equation (80), it may be assumed unity without loss of generality. The heating rate ratio of Equation (80) must be unity to produce a constant heating rate over the surface.

Defining

$$g(\theta) = \cos^2\theta \left(1-\cos^2 2\beta^2\theta\right)^{\frac{1}{2}} \tag{81}$$

gives the equation for a constant heating rate surface (after squaring)

$$\beta 2^{n+1} \int_0^s y^{2n}\, g(\theta)\, ds = g^2(\theta)\, y^{2n} \tag{82}$$

Differentiation produces

$$\frac{dg}{d\theta}\frac{d\theta}{ds} = \beta 2^n - \frac{ng}{y}\frac{dy}{ds} \tag{83}$$

Thus

$$\frac{ds}{d\theta} = \frac{\frac{dg}{d\theta}}{\beta 2^n - \frac{ng}{y}\cos\theta} \quad . \tag{84}$$

The geometric relationships of x, y, s, θ are as follows:

$$\frac{dx}{d\theta} = \sin\theta \frac{ds}{d\theta} \tag{85}$$

$$\frac{dy}{d\theta} = \cos\theta \frac{ds}{d\theta} \tag{86}$$

or after substitution of Equation (81) into Equation (84)

$$\frac{ds}{d\theta} = \frac{\sin\theta\cos\theta\left[\frac{(2+\beta^2)\cos^{2\beta^2}\theta - 2}{(1-\cos^{2\beta^2}\theta)^{\frac{1}{2}}}\right]}{\beta 2^n - \frac{n}{y}\cos^3\theta\left(1-\cos^{2\beta^2}\theta\right)^{\frac{1}{2}}} \quad . \tag{87}$$

By simultaneous integration of Equations (85), (86), and (87) with the initial boundary conditions that x = 0 and y = 0 at θ = 0, numerical solutions were obtained for two and three dimensional cases (n = 0 and 1, respectively) and for γ of 1.4. Numerical results are tabulated in Table 1.

In Table 1, note the small percentage difference between the optimum geometry for two and three dimensional surfaces. The heating rate distribution on the optimum surfaces are within 3 percent of the distribution for a 2:1 ellipse (minor axis parallel to the velocity vector). Therefore, for simplification, the nose and leading edge optimum geometry will be constructed as a 2:1 ellipse. From Table 1, also note that beyond a slope of 36° the radius of curvature becomes negative (a cusp occurs) and the optimum surface can no longer be maintained. It can be shown from Equation (80) that attaching the optimum surface to the remainder of the vehicle with a smooth curve of positive radius of curvature will insure that at no point will the stagnation region temperature be exceeded.

TABLE I

CONSTANT TEMPERATURE SURFACE GEOMETRY

$\gamma = 1.4$; $\beta = 0.53452$

θ (DEGREES)	n = 0			n = 1		
	$\frac{x}{R_s}$	$\frac{y}{R_s}$	$\frac{1}{R_s}\frac{ds}{d\theta}$	$\frac{x}{R_s}$	$\frac{y}{R_s}$	$\frac{1}{R_s}\frac{ds}{d\theta}$
0	0	0	1.00000	0	0	1.00000
2	$.60794^{-3}$	$.34779^{-1}$	.99659	$.60795^{-3}$	$.34854^{-1}$	.99608
4	$.24182^{-2}$	$.69342^{-1}$	.98570	$.24169^{-2}$	$.69393^{-1}$	.98438
6	$.53893^{-2}$	.10332	.97031	$.53820^{-2}$	.10331	.96502
8	$.94527^{-2}$	.13644	.94631	$.94298^{-2}$	.13630	.93817
10	$.14514^{-1}$	.16842	.91552	$.14459^{-1}$	.16807	.90413
12	$.20456^{-1}$	.19900	.87820	$.20345^{-1}$	.19837	.86325
14	$.27137^{-1}$	.22796	.83464	$.26936^{-1}$	.22695	.81593
16	$.34397^{-1}$	.25508	.78520	$.34066^{-1}$	.25358	.76269
18	$.42058^{-1}$	.28015	.73028	$.41549^{-1}$	.27807	.70409
20	$.49930^{-1}$	.30303	.67032	$.49188^{-1}$	.30028	.64075
22	$.57808^{-1}$	.32358	.60583	$.56779^{-1}$	.32007	.57339
24	$.65484^{-1}$	.34168	.53733	$.64114^{-1}$	.33737	.50274
26	$.72744^{-1}$	.35726	.46538	$.70987^{-1}$	.35213	.42963
28	$.79374^{-1}$	.37029	.39059	$.77198^{-1}$	.36433	.35489
30	$.85165^{-1}$	.38076	.31358	$.82558^{-1}$	.37402	.27942
32	$.89914^{-1}$	.38868	.23500	$.86897^{-1}$	.38126	.20413
34	$.93431^{-1}$	.39411	.15552	$.90064^{-1}$	.38615	.12995
36	$.95541^{-1}$	.39713	$.75814^{-1}$	$.91933^{-1}$	.38883	$.57809^{-1}$
37.719				$.92429^{-1}$	.38950	$-.18802^{-2}$
38	$.96085^{-1}$	.39787	$-.12637^{-1}$			

SECTION 4

OPTIMIZATION OF COMPOSITE CONFIGURATION

4-A. Introduction

In the preceding Section 3, we showed that the maximum hypersonic L/D may be achieved by a vehicle with the following characteristics:

1. Flat bottom surface
2. Clipped delta planform with a 0.32 taper ratio
3. Outboard dorsal delta fins
4. Elliptical (2:1) nose and leading edges

In this section the composite configuration will be optimized for maximum hypersonic L/D, which satisfies the 11 constraint conditions delineated in Section 2.

These constraint equations are summarized as follows:

$$\frac{1}{2}\rho V^2 = \frac{W}{SC_L}\left(1 - \frac{V^2}{V_c^2}\right) \tag{88}$$

$$W = \text{fixed value} \tag{89}$$

$$\frac{W}{SA} = 50 \text{ pounds per square foot} \tag{90}$$

$$T_N = \text{fixed value} \tag{91}$$

$$T_{LE} = \text{fixed value} \tag{92}$$

$$T_{FLE} = \text{fixed value} \tag{93}$$

$$T_{LS} = \text{fixed value} \tag{94}$$

$$C_{l_\beta} = 0 \tag{95}$$

$$C_{m_\alpha} = 0 \tag{96}$$

$$C_{n_\beta} = 0 \tag{97}$$

$$\frac{S_F}{S} = 0.1\ . \tag{98}$$

The available equations from which a solution may be attempted will now be reviewed.

4-B. Available Equations

In Appendix II, the temperature Equations (155), (169), (170), and (172) were derived. They are summarized here in functional form:

$$T_N = f\left(\frac{W}{S}, C_L, R_N\right) \tag{99}$$

$$T_{LE} = f\left(\frac{W}{S}, C_L, R_{LE}, \Lambda, \alpha\right) \tag{100}$$

$$T_{FLE} = f\left(\frac{W}{S}, C_L, R_F, \Lambda_F, \alpha\right) \tag{101}$$

$$T_{LS} = f\left(\frac{W}{S}\right); \tag{102}$$

The hypersonic aerodynamic equations are compiled in Appendix III, Equations (190) through (216).

$$\left[C_A, C_N, C_m, C_{Y\beta}, C_{\ell\beta}, C_{n\beta}\right] =$$

$$f\left[R_N, R_{LE}, R_F, x_N, x_{LE}, x_L, x_F, x_{FLE}, y_{LE}, y_F, z_N, z_{LE}, z_L, z_F, z_{FLE},\right.$$

$$\left.\ell_{LE}, \ell_F, S_F, S_L, S_W, \lambda, \Lambda, \Lambda_F, S, b, c, \bar{c}, \alpha, V_\infty, \nu_\infty\right]. \tag{103}$$

The aerodynamic characteristics as shown are a function of 30 variables, and since only 11 constraint equations are available, obviously additional auxiliary relationships are required. For the geometry shown in Figure 3, the following geometric relationships may be obtained:

$$c^2 = S\left[(1-m^2)\cot\Lambda + m^2\tan\lambda\right]^{-1} \tag{104}$$

$$b = 2c\left[(1-m)\cot\Lambda + m\tan\lambda\right] \tag{105}$$

$$\cot\Lambda_F = \frac{2S_F}{m^2c^2} \tag{106}$$

$$\bar{c} = \frac{2}{3}c \tag{107}$$

$$S_W = 2S \tag{108}$$

$$S_L = S - 2\ell_{LE}R_{LE} \tag{109}$$

$$\ell_{LE} = \frac{b}{2\cos\Lambda} \tag{110}$$

$$\ell_F = \frac{mc}{\sin\Lambda_F} \tag{111}$$

$$y_{LE} = \frac{b}{4} - R_{LE} \tag{112}$$

$$y_F = \frac{b}{2} \tag{113}$$

$$z_N = z_{cg} - R_N \tag{114}$$

$$z_{LE} = z_{cg} - R_{LE} \tag{115}$$

$$z_L = z_{cg} \tag{116}$$

$$z_F = z_{cg} - \frac{1}{3} mc \cot \Lambda_F \tag{117}$$

$$z_{FLE} = z_{cg} - \frac{1}{2} mc \cot \Lambda_F \tag{118}$$

$$x_N = x_{cg} \tag{119}$$

$$x_{LE} = x_{cg} - \frac{b}{4} \tan \Lambda \tag{120}$$

$$x_F = x_{cg} - (1 - \frac{1}{3} m) c \tag{121}$$

$$x_{FLE} = x_{cg} - (1 - \frac{1}{2} m) c \tag{122}$$

$$\frac{x_L}{c} = \frac{x_{cg}}{c} - 1 + \frac{(1-m)\left(\frac{1+2m}{3}\right) + m^2 + \frac{m^3 \tan \lambda}{2(1-m)\cot \Lambda}}{1 + m + \frac{m^2 \tan \lambda}{(1-m)\cot \Lambda}} \tag{123}$$

In addition, the kinematic viscosity, ν_∞, may be expressed as a function of altitude as follows:

$$\nu_\infty = \frac{\mu_\infty}{\rho_\infty} \; ; \; \mu_\infty \cong 3 \times 10^{-7} \text{ lb sec./ft}^2 \text{ in the altitude reigon of interest}$$

or

$$\nu_\infty = f(\rho_\infty). \tag{124}$$

Therefore, when the geometric relationships are used, the 11 constraint equations and the equation for $(L/D)_{max}$ may be expressed by the following independent variables:

1. W	5. R_F	9 m	13. ρ_∞
2. $\frac{W}{S}$	6. Λ	10. x_{cg}	14. α
3. R_N	7. Λ_F	11. z_{cg}	
4. R_{LE}	8. λ	12. V_∞	

Since 12 equations exist with 14 variables, two additional equations or conditions are required. The velocity for which the peak aerodynamic heating occurs (V = 21,170 feet per second, Equation 163 of Appendix II) is the critical design point and, hence, the vehicle must be constructed so as not to exceed the temperature at that point. Thus

$$V = 21,170 \text{ feet per second} \tag{125}$$

is one additional condition.

From the preceding section, the optimum taper ratio (m) for minimum leading edge drag was ascertained as 0.32. Hence, the final condition is that

$$m = 0.32 . \tag{126}$$

The problem now is properly set whereby the 11 constraint equations and the maximum L/D condition are expressible by 12 independent variables. When these 11 equations are solved simultaneously and the optimization process is imposed, a solution may be obtained.

4-C. Numerical Solutions

Because of the complex interrelationship of the 11 constraint equations, an iteration procedure was established to obtain a solution of the system. The aerodynamic equations were programmed on the IBM 7090 computer at ASD. The geometric quantities were computed for the condition of fixed weight and temperature as shown in Figure 5 in block diagram form (trial values of α_{opt}, x_{cg}, λ, and z_{cg} were required to initiate the program). A complete set of aerodynamic characteristics was obtained from the IBM 7090 computer for every degree of α from 7° to 30°. By inspection of the readout data, the angle of attack for $(L/D)_{max}$ was ascertained. The new radii were computed for the fixed temperatures and for the adjusted $C_{L_{opt}}$ and α_{opt} values (constraint Equations 91, 92, 93). A new equilibrium altitude was computed from constraint Equation (88). The vehicle was rendered neutrally stable (constraint Equations 96, 97, 95) by relocating the center of gravity and adjusting the fin toe-in angle (λ) as follows:

$$\frac{\Delta x_{cg}}{\bar{c}} = \frac{C_{m_\alpha}}{C_{N_\alpha}} . \tag{127}$$

$$\Delta\lambda = \frac{C_{n_\beta}}{8 \frac{x_F}{b} \frac{S_F}{S} \cos\alpha} \tag{128}$$

and

$$\frac{\Delta z_{cg}}{b} = \frac{-C_{\ell_\beta}}{C_{Y_\beta}} . \tag{129}$$

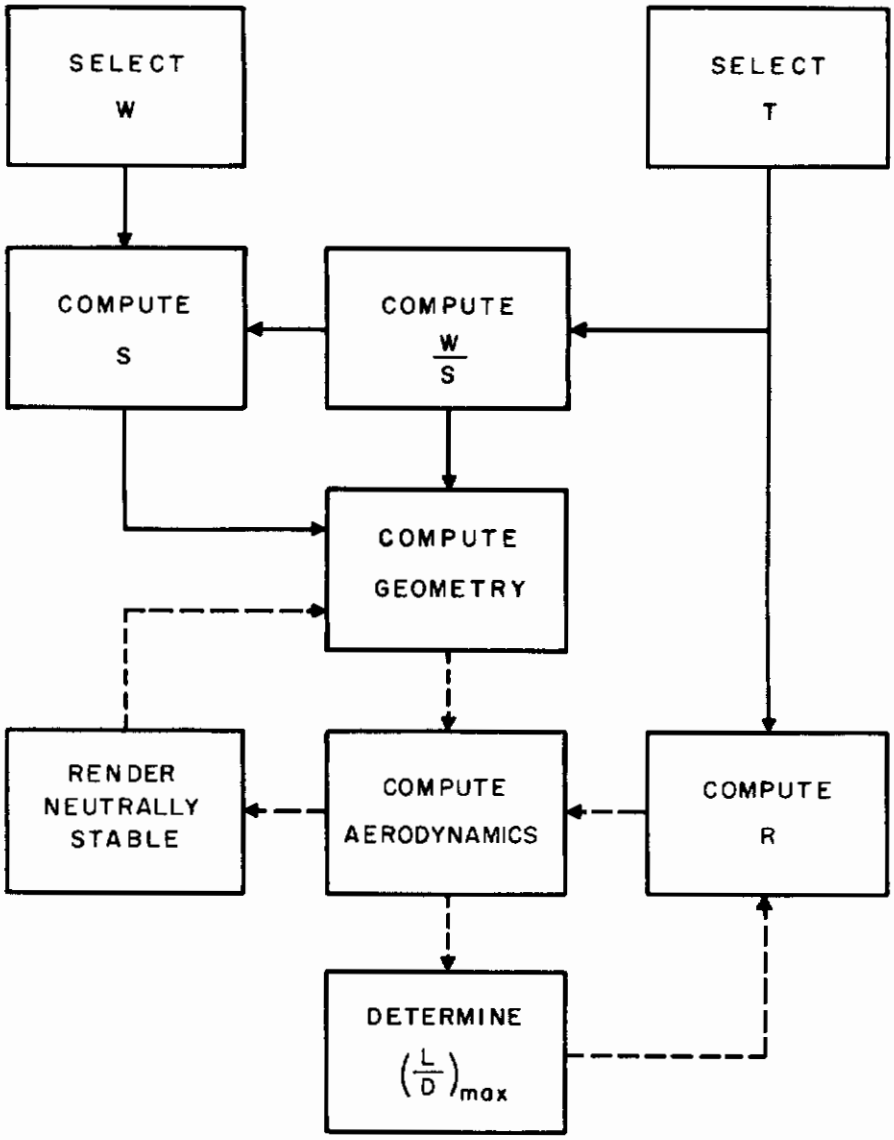

Figure 5. Block Diagram of Configurational Optimization Process

Additional geometric quantities were adjusted to conform with the four constraints of $\frac{S_F}{S} = 0.1$, $\frac{W}{S}$ = fixed through T_{LS}, $\frac{W}{S\,AR}$ = 50 pounds per square foot and W = fixed (Equations 98, 94, 90, 89). This procedure was continued until satisfactory convergence was obtained. The criteria for satisfactory convergence was that the aerodynamic center in all three axes be within 1 percent of reference length ($\bar{c}$ or b) from the c.g. and that the design angle of attack (α_{opt}) be within one degree of the iterated value. Approximately 10 successful iterations were required to produce satisfactory convergence. It was also

ascertained that most successful convergence was obtained by adjusting one quantity at a time in the following sequence:

1. α_{opt}
2. Δx_{cg}
3. $\Delta \lambda$
4. Δz_{cg}

Solutions were obtained at three temperatures (or wing loadings) for two vehicle weights of 10,000 and 100,000 pounds. Since four temperature locations were examined (nose, wing leading edge, fin leading edge, and lower surface), some assumption concerning the material construction was required. To minimize the number of cases to be examined, we assumed that the lower surface, wing leading edge, and fin leading edge were constructed of the same materials. That is

$$\dot{q}_{LS} = \dot{q}_{LE} = \dot{q}_{FLE} \quad . \tag{130}$$

In addition we assumed that the minimum lower surface temperature as computed from the wing loading value (Equation 172, Appendix II, or Figure 15) was the design limit. In other words no excess temperature capability was built into the vehicle and hence it is considered to be a minimum temperature design.

The nose of the vehicle represents a small portion of the vehicle's weight yet influences the value of $(L/D)_{max}$ greater than any other component of similar area. Therefore, a higher temperature capability for the nose than the remainder of the configuration results in huge dividends in hypersonic L/D, with only a minor penalty in weight. As stated in Appendix II, nose-cap materials have temperature capabilities in the vicinity of 4000°F while lower surface materials of lighter weight are limited to about 3000°F. For this case,

$$\dot{q}_N = 3\,\dot{q}_{LS} \quad . \tag{131}$$

Hence, in all numerical cases investigated, the nose was assumed to possess a heating rate limit that was three times as great as the remainder of the vehicle.

The characteristics of the optimized vehicles for the conditions cited are shown in Tables 2 and 3. The values of $(L/D)_{max}$ versus $\frac{W}{S}$ for these two classes of weight are presented in Figure 6. Note that the L/D increases with weight and decreases with wing loading although the temperature limits were constrained to increase with $\frac{W}{S}$ (as dictated by Equation 172, Appendix II). Hence the decrease of L/D with increasing wing loading would be even more drastic for a constant temperature constraint.

After the optimization process is complete, there are always interesting "tradeoffs" that should be investigated to determine the penalty incurred by various constraints. For this reason the maximum L/D was recomputed for the optimized configurations with the exception that the following quantities were removed:

Fin → 0; no stability constraint

TABLE 2

CHARACTERISTICS OF THE OPTIMUM LIFTING CONFIGURATIONS : W = 10,000 POUNDS

m = 0.32, S_F / S = 0.1, V = 21,170 ft/sec., and b = 14.14 ft

Characteristics	W/S (lb/sq ft) at		
	22.8	52.6	76.7
Λ (degrees)	82.8	69.2	57.9
Λ_F (degrees)	76.4	55.2	42.0
λ (degrees)	5.90	8.50	7.80
R_N (ft)	1.54	0.67	0.34
R_{LE} (ft)	0.51	0.60	0.61
R_F (ft)	0.03	0.28	0.29
c (ft)	59.4	23.1	15.0
$\frac{x_{cg}}{c}$	0.621	0.615	0.625
$\frac{z_{cg}}{b}$	0.173	0.158	0.177
$R_{e_\infty} \times 10^{-6}$	1.02	0.654	0.399
$\epsilon^{1/4} T_{LE}$ (°R)	2750	3250	3510
$\epsilon^{1/4} T_N$ (°R)	3620	4280	4610
α_{opt} (degrees)	14	17	23
$(L/D)_{max}$	2.08	1.75	1.29
C_N	0.152	0.219	0.369
$C_{Y\beta}$	− 0.205	− 0.340	− 0.365
C_m / C_N (percent)	− 0.90	0.27	0.82
$C_{m_\alpha} / C_{N_\alpha}$ (percent)	− 1.56	− 1.93	0.00
$C_{n_\beta} / C_{Y\beta}$ (percent)	0.65	− 0.35	− 0.88
$C_{l_\beta} / C_{Y\beta}$ (percent)	0.05	− 0.54	0.27

TABLE 3

CHARACTERISTICS OF THE OPTIMUM LIFTING CONFIGURATIONS: W = 100,000 POUNDS

m = 0.32, S_F/S = 0.1, V = 21,170 ft/sec., and b = 44.72 ft

Characteristics	W/S (lb/sq ft) at		
	17.6	45.7	71.0
Λ (degrees)	82.8	69.2	57.8
Λ_F (degrees)	77.0	55.8	41.9
λ (degrees)	2.75	4.30	4.00
R_N (ft)	3.30	1.14	0.48
R_{LE} (ft)	0.63	0.87	0.77
R_F (ft)	0.05	0.67	0.51
c (ft)	219	79.2	49.6
$\frac{x_{cg}}{c}$	0.642	0.622	0.645
$\frac{z_{cg}}{b}$	0.186	0.162	0.224
$R_{e_\infty} \times 10^{-6}$	5.33	3.03	1.62
$\epsilon^{1/4} T_{LE}$ (°R)	2610	3160	3450
$\epsilon^{1/4} T_N$ (°R)	3440	4160	4540
α_{opt} (degrees)	10	13	18
$(L/D)_{max}$	3.26	2.54	1.88
C_N	0.087	0.133	0.235
C_{Y_β}	- 0.075	- 0.148	- 0.155
C_m/C_N (percent)	0.63	- 0.03	0.80
$C_{m_\alpha}/C_{N_\alpha}$ (percent)	0.42	- 0.23	1.21
C_{n_β}/C_{Y_β} (percent)	0.32	- 0.23	- 0.69
$C_{\ell_\beta}/C_{Y_\beta}$ (percent)	0.64	0.22	- 0.99

$C_f \rightarrow 0$; inviscid

All R $\rightarrow$ 0; no thermal constraint.

These data are presented in Figure 7 for vehicles of the 10,000-pound weight class and in Figure 8 for the 100,000-pound vehicles. Note that the temperature constraint is the most severe, while the skin friction is next most limiting for both weight classes.

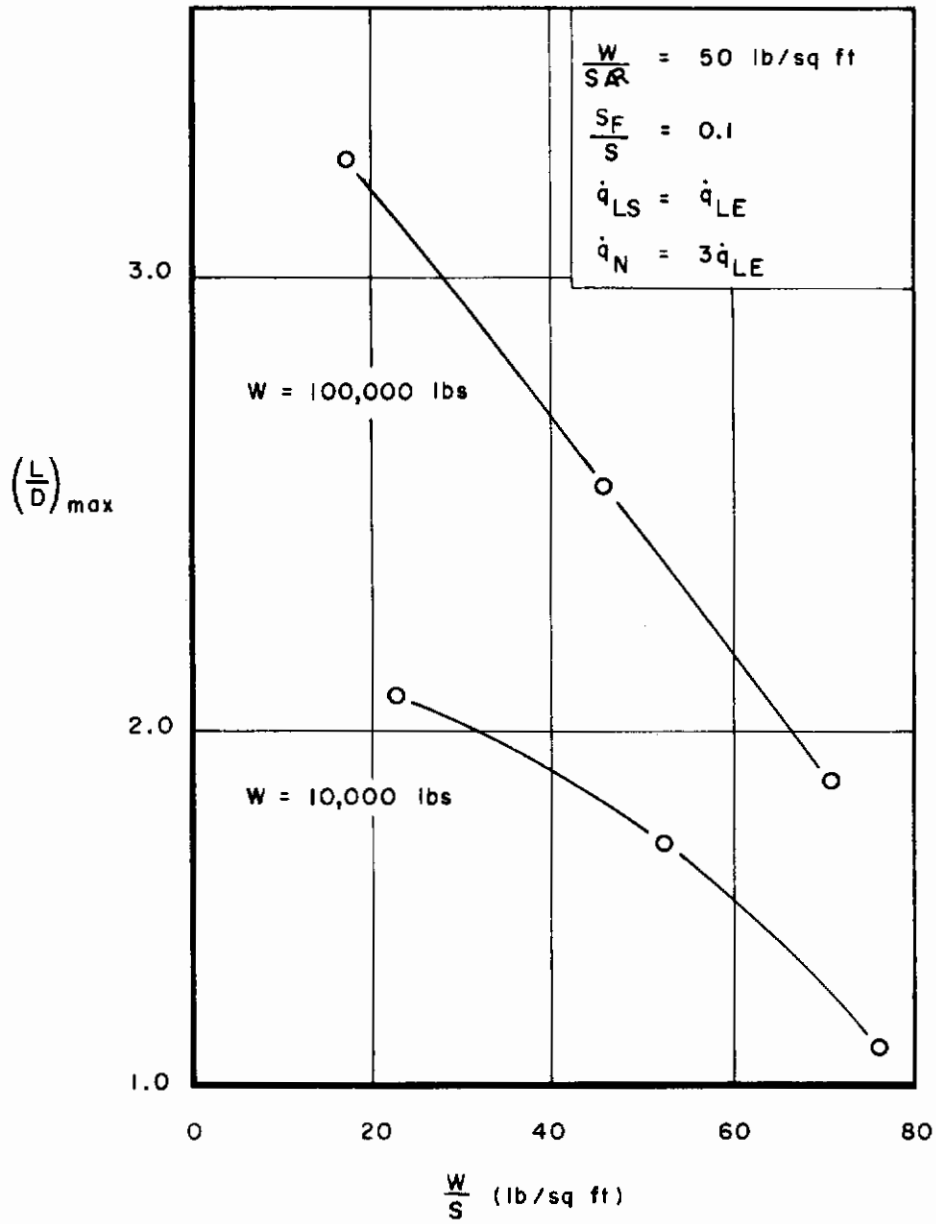

Figure 6. Maximum L/D Versus Wing Loading

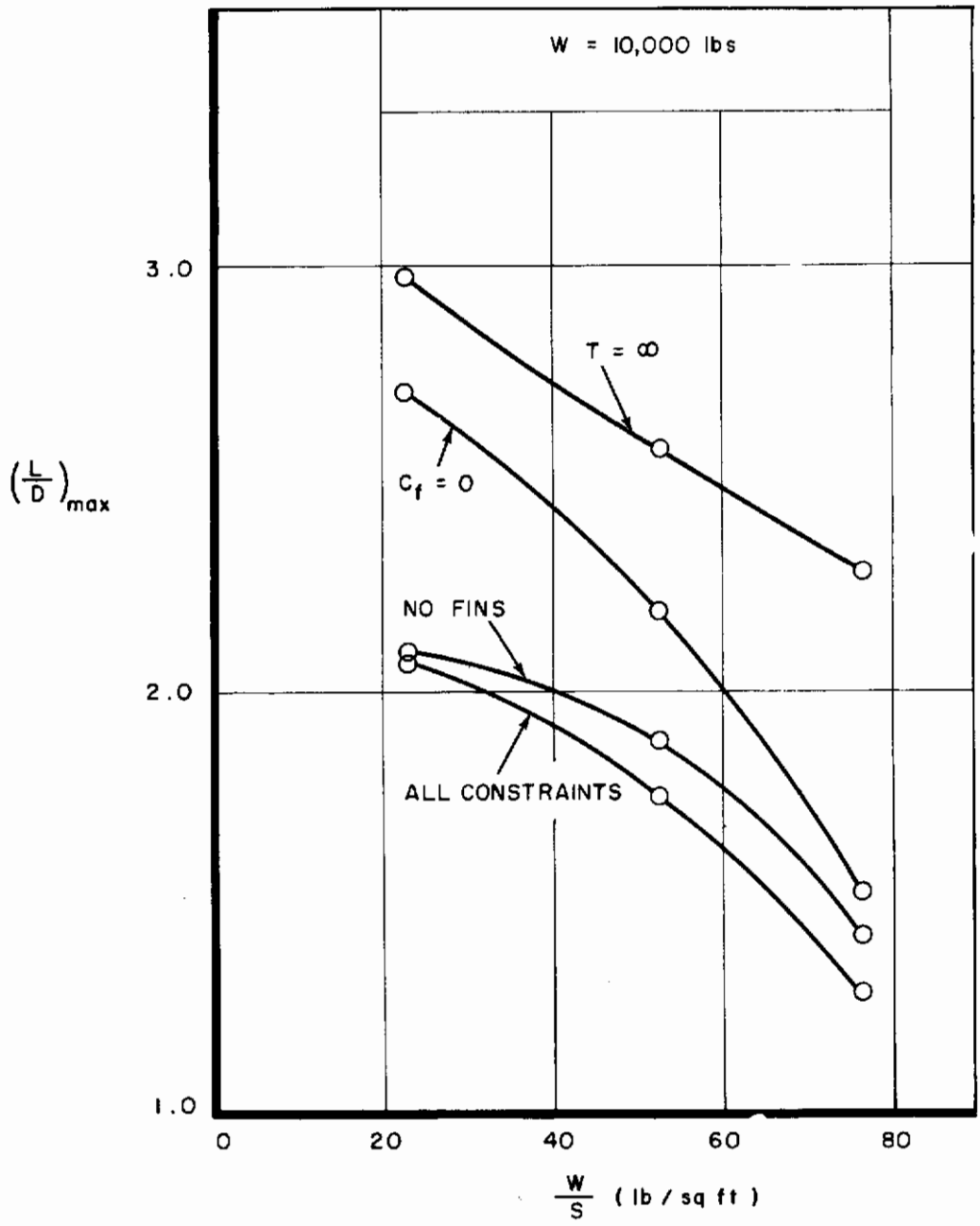

Figure 7. Constraint Influence on $(L/D)_{max}$; W = 10,000 Pounds

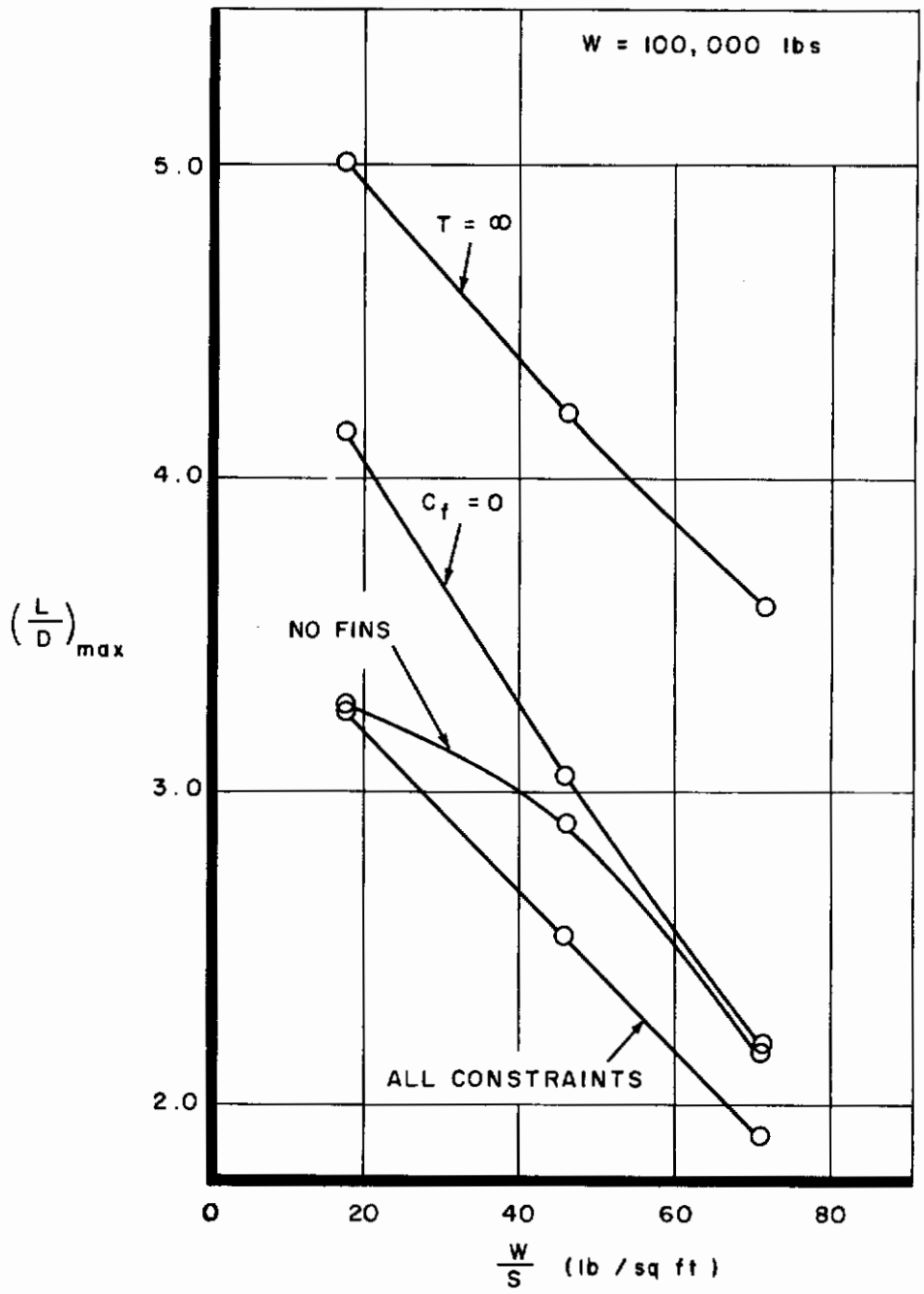

Figure 8. Constraint Influence on $(L/D)_{max}$; W = 100,000 Pounds

4-D. Upper Surface Design

In the preceding paragraphs the optimum vehicle characteristics for a lifting re-entry vehicle were determined. Throughout the analysis only the planform and lower surface geometry were discussed. The lower surface geometry is designed by the hypersonic characteristics leaving the upper surface free for the designer to achieve satisfactory low-speed characteristics while meeting the volume and booster attachment constraints. A cambered upper surface that locates the low-speed center of pressure aft of the hypersonically constrained c.g. and minimizes profile drag, achieves optimum low-speed performance and stability. However, the volume and attachment constraints may alter this contour in various degrees. A complete analysis of this problem is not warranted here, in that infinite possibilities exist; however, a typical complete configuration is shown as an example.

One of the 100,000-pound configurations ($\frac{W}{S}$ = 45.7 pounds per square foot) is shown in Figure 9 with a cambered modified Clark-Y profile upper surface. All constrained geometric quantities are shown, and a cylindrical aft fuselage is depicted unexposed to the aerodynamic heating to contain the payload volume and c.g. while providing an interface for booster attachment.

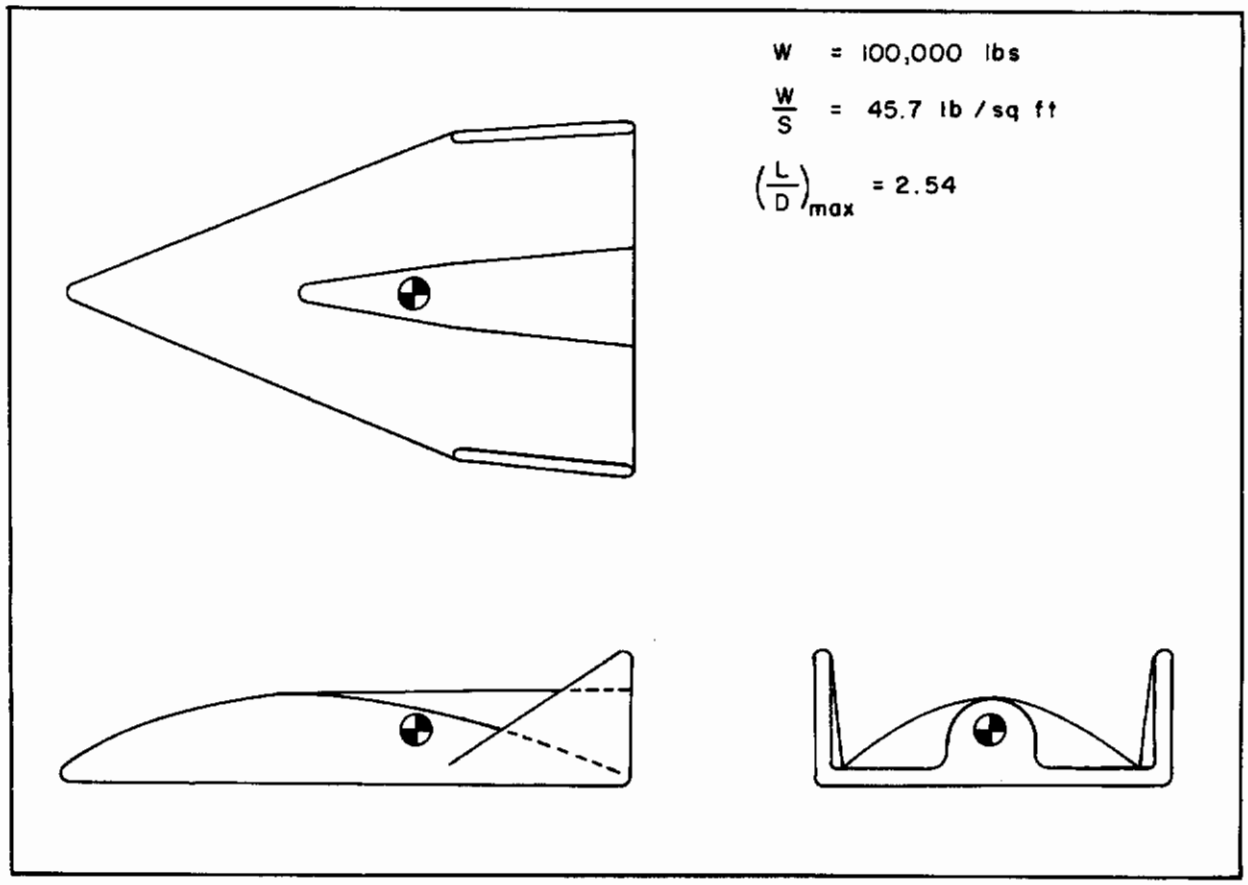

Figure 9. Typical Optimum Geometry

4-E. Range Modulation

Throughout the entire investigation, the vehicle has been designed for one attitude; that is, the angle of attack for $(L/D)_{max}$. Heating, stability, internal heat protection, control surface, sizing, etc. have been determined for this condition. However, L/D must be adjusted from the maximum value to some lower value to modulate longitudinal range. The degree of range modulation depends upon the ratio of the maximum L/D to the minimum value. L/D modulation may be achieved by opening a speed brake to increase drag at constant angle of attack. Symmetrical deflection of the rudders may accomplish this feat if sufficient temperature capability exists. Table 4 expresses the values of L/D for rudder deflections of 45° for the configurations studied. The rudder area was assumed to be one-half of the fin area.

TABLE 4

VALUES OF L/D FOR RUDDER DEFLECTIONS

$S_R = 0.5\ S_F$ AND $S_F = 0.1\ S$

W (POUNDS)	W/S (LB PER SQ FT)	α_{opt} (DEGREES)	$\delta_R = 0°$ $(L/D)_{max}$	$\delta_R = 45°$ $(L/D)_{min}$
10,000	22.8	14	2.080	0.703
10,000	52.6	17	1.751	0.802
10,000	76.7	23	1.287	0.805
100,000	17.6	10	3.263	0.533
100,000	45.7	13	2.543	0.701
100,000	71.0	18	1.883	0.868

SECTION 5

CONCLUSIONS

The objective of this investigation was to optimize lifting re-entry configurations for the following set of requirements:

1. Achieve successful manned re-entry from circular speeds
2. Provide large lateral maneuverability and longitudinal range modulation
3. Provide satisfactory landing characteristics
4. Protect the vehicle from the aerodynamic heating
5. Provide the vehicle with adequate stability to produce satisfactory handling qualities

These requirements were converted into the 11 property constraints for the vehicle. With the constraint equations formulated, the configuration was designed for maximum hypersonic L/D after it was shown that the greatest lateral and longitudinal range might be achieved by maximizing hypersonic L/D.

The geometry of a generalized configuration was optimized for maximum L/D and the following characteristics obtained:

1. Flat bottom lower surface
2. Clipped delta planform with a 0.32 taper ratio
3. Delta dorsal vertical fins
4. (2:1) elliptical nose and leading edges

With the general configurational geometry established, the $(L/D)_{max}$ was determined for the composite detailed geometry for two vehicle weight classes (10,000 and 100,000 pounds) while meeting the previously established 11 constraints. For the domain investigated, these numerical results show that low aspect ratios, low wing loadings, and large scale vehicles produce the highest L/D. Also the temperature constraint for the domain investigated is the most severe in limiting L/D. Subsequent to the temperature constraint, the effects of skin friction are the next most limiting. Therefore, with the development of drastically improved materials and the relaxation of the thermal constraint, higher L/D values are possible. In addition, as booster payload capability increases and the structural designs become more efficient (reducing $\frac{W}{S}$) higher values of L/D may be anticipated.

APPENDIX I

TRAJECTORY ANALYSIS

The trajectory must be computed first to optimize the performance of a vehicle.

The equations of motion for a banked, gliding, re-entry vehicle are listed as follows:

$$m\dot{V} = -D - mg \sin\gamma \tag{132}$$

$$mV\dot{\gamma} = L\cos\phi + \frac{mV^2\cos\gamma}{R_E} - mg\cos\gamma \tag{133}$$

$$mV\dot{\psi} = \frac{L\sin\phi}{\cos\gamma} \tag{134}$$

For hypersonic lifting re-entry, the assumption of γ and $\dot{\gamma}$ equal zero may be used. Thus

$$\frac{\dot{V}}{g} = -\frac{D}{W} \tag{135}$$

$$\frac{L}{W}\cos\phi = 1 - \frac{V^2}{V_c^2} \quad ; \text{ where } V_c^2 = g R_E \tag{136}$$

$$\frac{V\dot{\psi}}{g} = \frac{L}{W}\sin\phi \, . \tag{137}$$

The range equations are as follows:

$$\text{Longitudinal range} = R_x = \int V\cos\psi\, dt = \int_{V_i}^{0} V\cos\psi\,\frac{dV}{\dot{V}} \tag{138}$$

$$\text{Lateral range} = R_y = \int V\sin\psi\, dt = \int_{V_i}^{0} V\sin\psi\,\frac{dV}{\dot{V}} \tag{139}$$

where

$$\psi = \int \dot{\psi}\, dt = \int_{V_i}^{V} \frac{\dot{\psi}}{\dot{V}}\, dV \, . \tag{140}$$

When the equations of motion (135) and (137) are used,

$$\psi = -\int_{V_i}^{V} \frac{L}{D}\sin\phi\,\frac{dV}{V} \tag{141}$$

Integrating Equation (141) for constant L/D and ϕ produces

$$\psi = \frac{L}{D}\sin\phi\,\ln\frac{V_i}{V} \tag{142}$$

Using Equations (135), (136), and (142) in Equations (138) and (139) results in

$$\frac{R_x}{R_E} = \int_0^{\frac{V_i}{V_c}} \frac{L}{D} \cos\phi \left(\frac{\frac{V}{V_c}}{1 - \frac{V^2}{V_c^2}} \right) \cos\left(\frac{L}{D} \sin\phi \ln \frac{V_i}{V} \right) d\left(\frac{V}{V_c} \right) \tag{143}$$

$$\frac{R_y}{R_E} = \int_0^{\frac{V_i}{V_c}} \frac{L}{D} \cos\phi \left(\frac{\frac{V}{V_c}}{1 - \frac{V^2}{V_c^2}} \right) \sin\left(\frac{L}{D} \sin\phi \ln \frac{V_i}{V} \right) d\left(\frac{V}{V_c} \right) . \tag{144}$$

Maximum longitudinal range achieved for zero bank angle ($\phi = 0$) in Equation (143) results in the following:

$$\left(\frac{R_x}{R_E} \right)_{max} = \frac{L}{D} \int_0^{\frac{V_i}{V_c}} \frac{x\,dx}{1 - x^2} = -\frac{1}{2} \frac{L}{D} \ln \left(1 - \frac{V_i^2}{V_c^2} \right) \tag{145}$$

where $x = \frac{V}{V_c}$, dummy variable.

Figure 10 shows a plot of the longitudinal range achieved for various initial velocities.

The integration of the lateral range equation is more involved, however. For $\frac{V_i}{V_c} = 1$,

$$\left(\frac{R_y}{R_E} \right) = \frac{L}{D} \cos\phi \int_0^1 \frac{x}{1 - x^2} \sin\left(-\frac{L}{D} \sin\phi \ln x \right) dx . \tag{146}$$

Transformation of variables permits integration. Let

$$y = -\ln x^2$$

and

$$a = \frac{1}{2} \frac{L}{D} \sin\phi .$$

Hence

$$\frac{\left(\frac{R_y}{R_E} \right)}{\frac{1}{2} \frac{L}{D} \cos\phi} = \int_0^\infty \frac{e^{-y} (\sin a y)}{1 - e^{-y}} dy = \int_0^\infty e^{-y} (\sin a y) \sum_{k=0}^{\infty} e^{-ky} dy \tag{147}$$

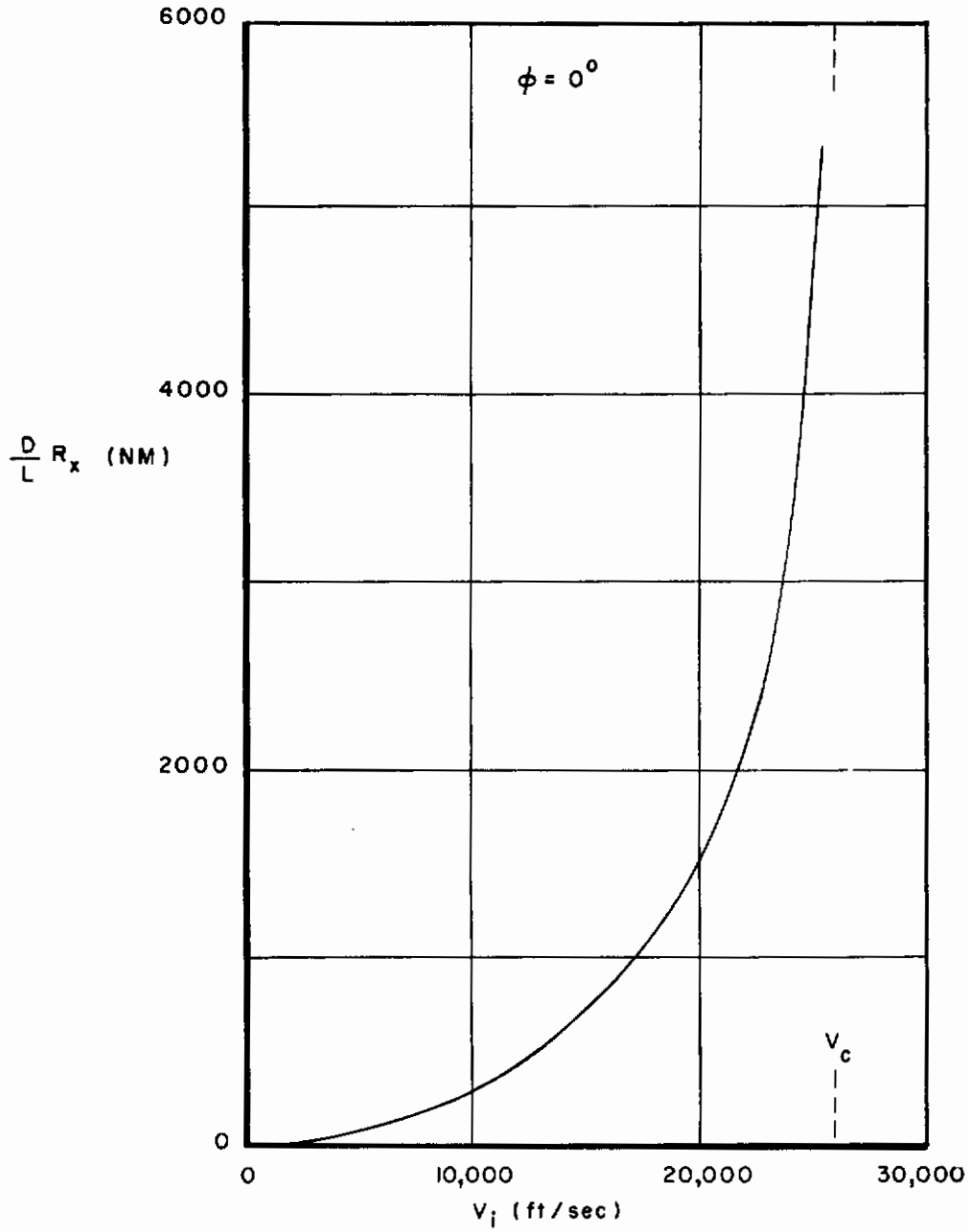

Figure 10. Longitudinal Range Versus Initial Velocity

When the numerator is replaced by a power series to permit integration and the order is changed,

$$\left(\frac{R_y}{R_E}\right) = \frac{1}{2} \frac{L}{D} \cos\phi \sum_{n=1}^{\infty} \int_0 e^{-ny} (\sin a\, y)\, dy \qquad (148)$$

and integrating Equation (148) produces

$$\left(\frac{R_y}{R_E}\right) = \cot\phi \sum_{n=1}^{\infty} \frac{a^2}{a^2 + n^2} . \tag{149}$$

In the region of interest ($0 < a < 2$), the series may be approximated as follows:

$$\left(\frac{R_y}{R_E}\right) \cong \frac{\left(\frac{L}{D}\right)^2 \sin 2\phi}{5.2\left[1 + 0.106\left(\frac{L}{D}\right)^2 \sin^2\phi\right]} \tag{150}$$

By means of differentiation, the optimum bank angle may be obtained to achieve maximum range as follows:

$$\cot^2\phi_{opt} = 1 + 0.106\left(\frac{L}{D}\right)^2 . \tag{151}$$

Figure 11 is a plot of optimum bank angle as a function of L/D as obtained from Equation (151). By insertion of Equation (151) into Equation (150) the maximum range for the optimum bank angle is obtained.

$$\left(\frac{R_y}{R_E}\right)_{max} = \frac{\left(\frac{L}{D}\right)^2}{5.2\sqrt{1 + 0.106\left(\frac{L}{D}\right)^2}} \tag{152}$$

Figure 12 presents maximum lateral range versus L/D as obtained for Equation (152).

It is apparent from Equation (145) or Figure 10 that maximum longitudinal range control is achieved by modulating L/D at hypersonic speeds. As apparent from Equation (152) or Figure 12, the maximum lateral range control can be achieved by maximizing L/D during re-entry. Thus, maximum maneuverability is achieved by maximizing hypersonic L/D.

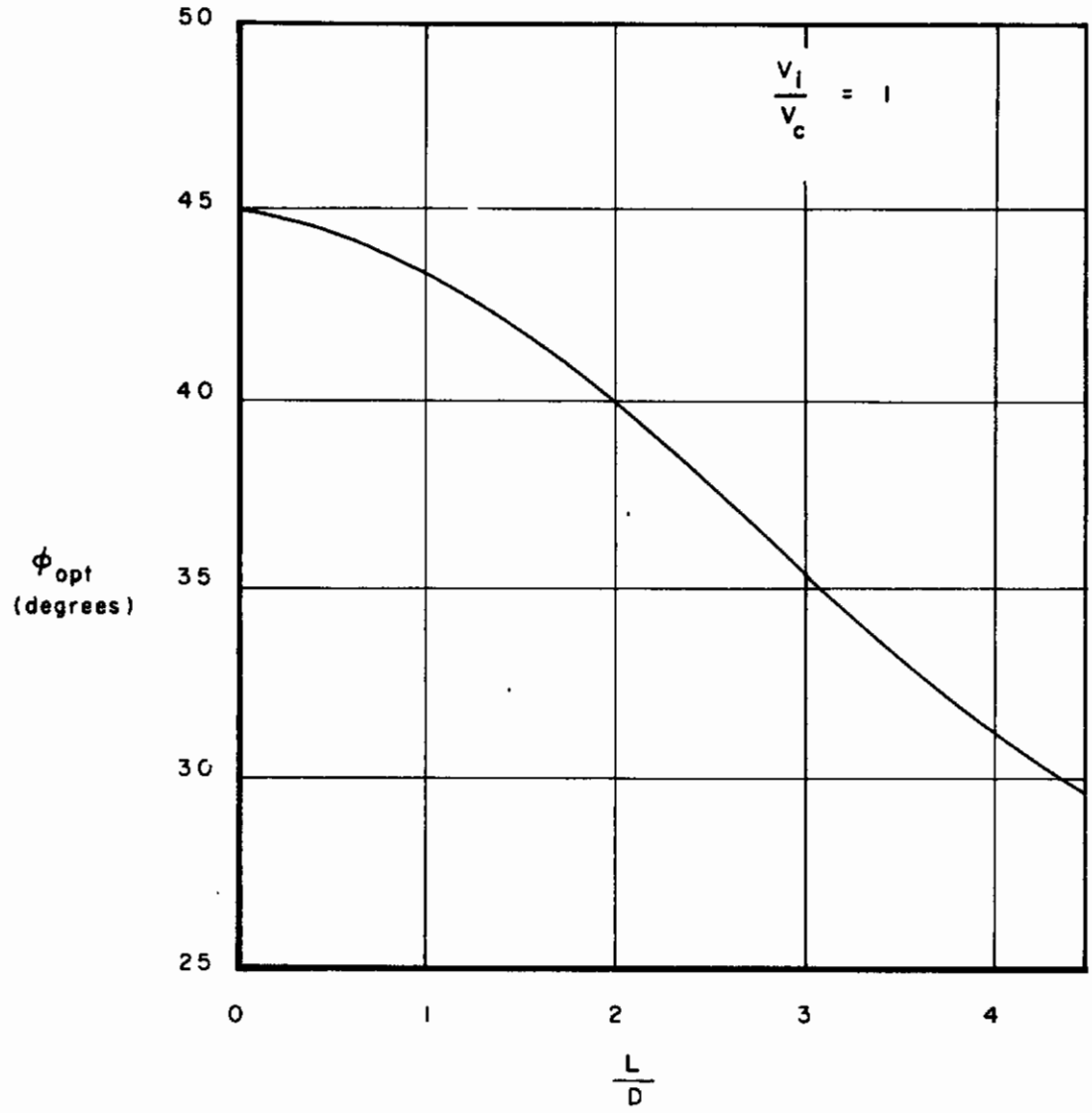

Figure 11. Optimum Bank Angle for Achieving Maximum Lateral Range

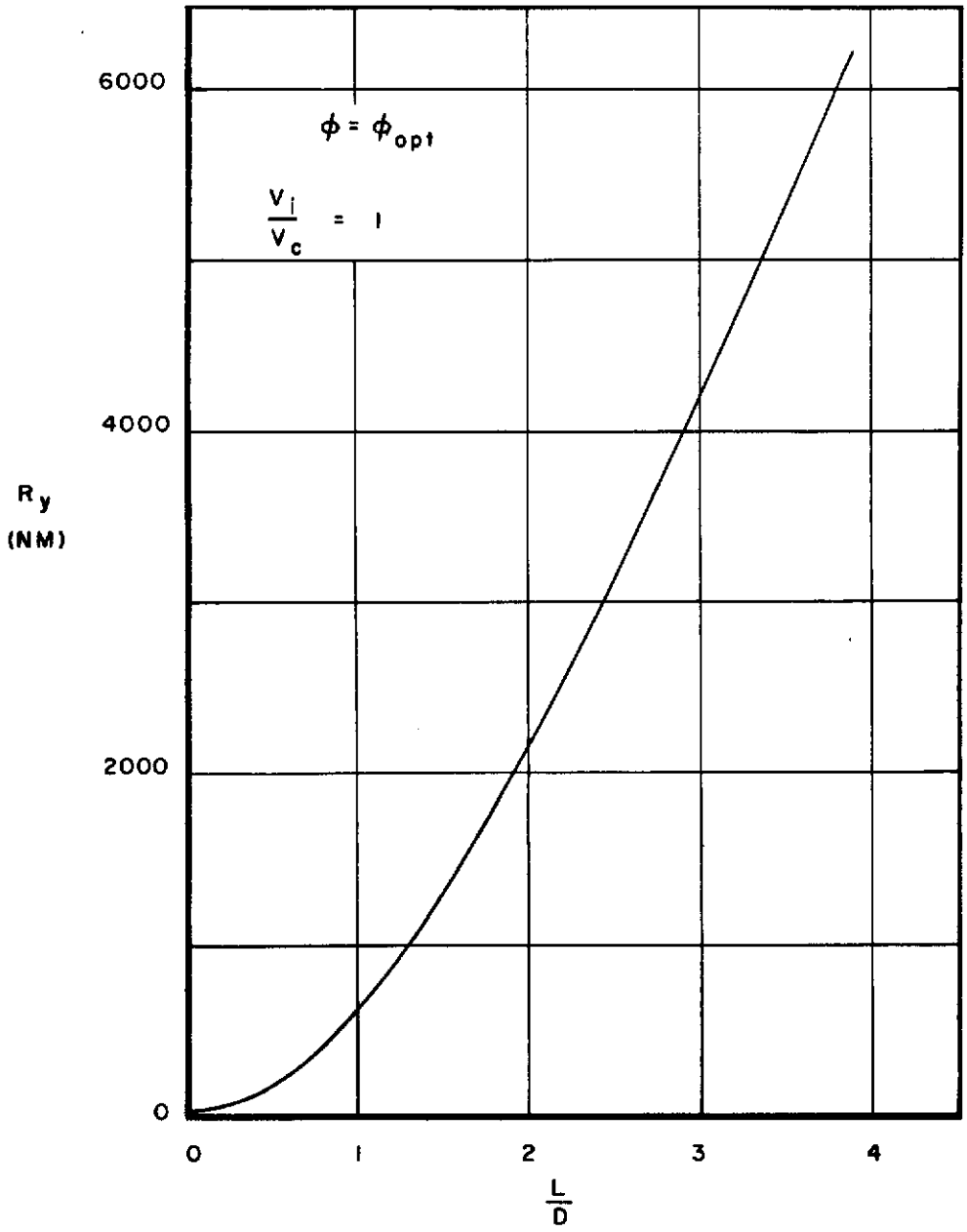

Figure 12. Maximum Lateral Range Versus L/D

APPENDIX II

HEAT TRANSFER ANALYSIS

II-A. Introduction

The design of hypervelocity re-entry vehicles depends vitally upon the heat transfer rates and temperatures that occur at critical points on the vehicle. The re-entry vehicle of the lifting or glide type experiences much less severe heating rates (tens of BTU/ft^2 sec.) than for the ballistic type (thousands of BTU/ft^2 sec.), but the total heat transferred is greater because of the extremely long flight times of the former in the atmosphere (about an hour as opposed to a few seconds). Because of this fact ablation techniques have not proved to be practical and a radiation-cooled structure is used. In lifting re-entry a steady-state thermal condition is quickly reached in which the influx of aerodynamic convective heating is balanced by the efflux of thermal radiation resulting in an equilibrium temperature of a surface. This temperature is maintained below the limit of the surface material (approximately 3000°F) by carefully designing the shape of the vehicle and designating flight paths that avoid the critical heating region.

The stagnation region usually experiences the highest heating rate on hypersonic vehicles. Many methods are available for predicting laminar heating rates at the stagnation point and these will be investigated with the objective of ascertaining the simplest method that possesses sufficient accuracy for the heating analysis.

The leading edge is the next most important area to be considered. Transformation is possible to convert from three dimensional to two dimensional stagnation heating. The leading edge geometry in section and planform dictates the heating rate distribution.

Next, the analysis of the lower surface aft of the nose and leading edge must be analyzed for both laminar and turbulent flow.

II-B. Stagnation Point Heating

Several of the available methods for computing stagnation heat-transfer rates were studied and computed for a typical lifting re-entry glide path ($\frac{W}{SC_L} = 100$) as shown in Figure 13. The methods analyzed are listed as follows:

1. Sibulkin
2. Cohen and Reshotko
3. Lees, approximate and exact
4. Detra, Kemp, and Riddell
5. Fay and Riddell

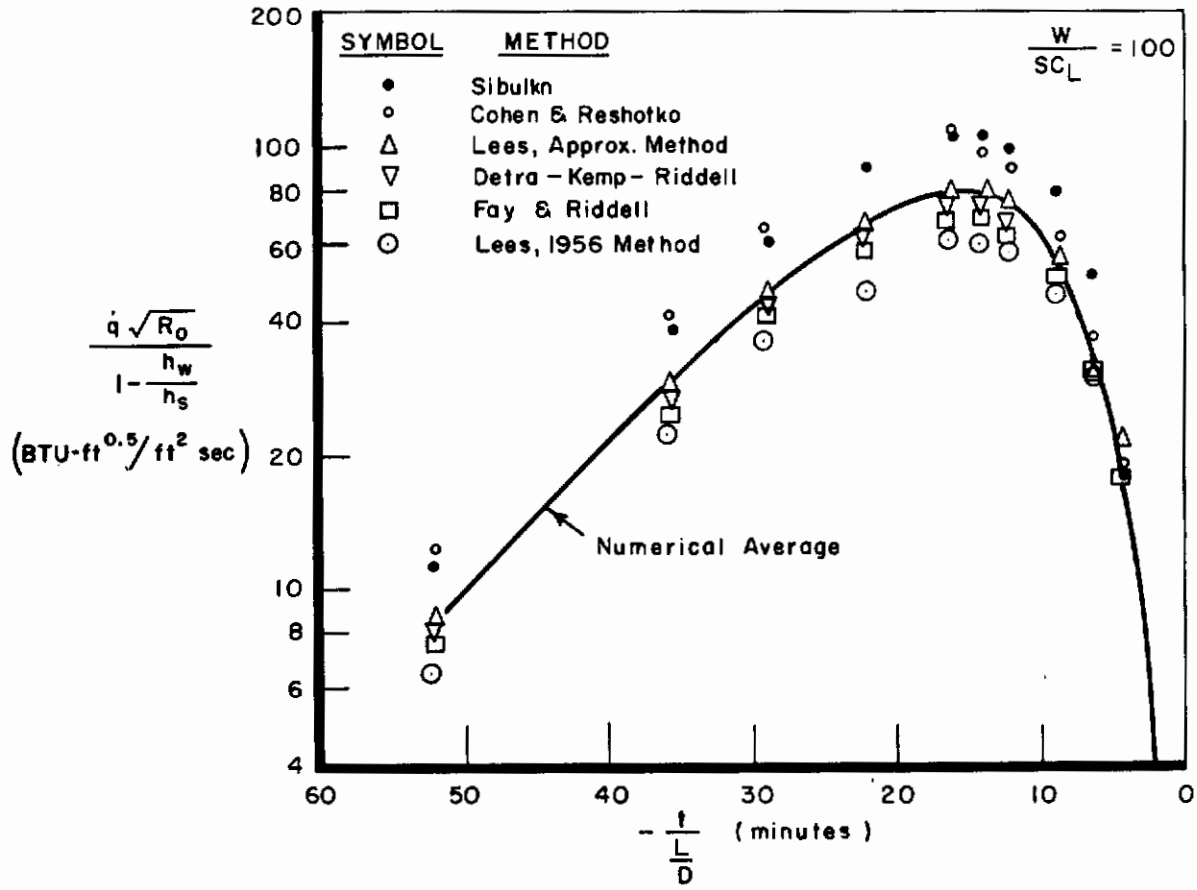

Figure 13. Comparison of the Stagnation-Point Heating Rate for Various Methods

The simplest method (Lees approximate) also is closest to the numerical average of all methods. For this reason Lees' approximate method in the following form was adopted:

$$\dot{q}_s = (15.5)\, 2^{\frac{n}{2}} \left(\frac{\rho_\infty}{R_N}\right)^{0.5} \left(\frac{V_\infty}{1000}\right)^3 \left(1 - \frac{h_w}{h_s}\right). \qquad (153)$$

II-3. Leading Edge Heating

The unswept leading edge may be obtained simply from Lees' stagnation equation for n = 0. The conversion for sweep as shown in Reference 5 is as follows:

$$\frac{\dot{q}_\Lambda}{\dot{q}_{\Lambda=0}} = \cos \Lambda_e \qquad (154)$$

where

$$\Lambda_e = \sin^{-1} (\sin \Lambda \cos \alpha)\,; \text{ for the wing leading edge} \qquad (155a)$$

or

$$\Lambda_e = \Lambda_F + \alpha \; ; \text{ for the fin leading edge.} \tag{155b}$$

Thus

$$\dot{q}_{LE} = \dot{q}_S \left(\frac{R_N}{2R_{LE}}\right)^{0.5} \cos \Lambda_e \tag{156}$$

II-4. Lower Surface Heating

The nose and leading edge are generally laminar at critical heating for "state of the art" materials, structures, and geometries. Aft of the leading edge local transition to turbulent flow may occur depending upon attitude, altitude, velocity, surface roughness, temperature, and geometry. As an allowance for a degree of conservatism, the lower surface will be designed for either laminar or turbulent flow at critical heating depending on which is higher.

The method adopted for computing heat transfer is the reference enthalpy technique first expressed by Eckert (Reference 6). Schmidt (References 7 and 8) and Hankey (Reference 5) have computed laminar and turbulent heat transfer to flat plates for re-entry flight conditions. An empirical approximation to these data applicable in the critical heating regime are tabulated as follows:

$$\dot{q}_{\text{Lam FP}} = \frac{12.1}{x^{0.5}} \left(\frac{V_\infty}{1000}\right)^3 \left(1 - \frac{h_w}{h_s}\right) \left(\rho_\infty \sin^2 \alpha \cos \alpha\right)^{0.5} \tag{157}$$

$$\dot{q}_{\text{Turb FP}} = \frac{4220}{x^{0.2}} \left(\frac{V_\infty}{1000}\right)^3 \left(1 - \frac{h_w}{h_s}\right) \left(\rho_\infty \sin^2 \alpha \cos \alpha\right)^{0.8}. \tag{158}$$

II-5. Critical Heating

For equilibrium glide (Appendix I) in which

$$\frac{1}{2} \rho_\infty V_\infty^2 = \frac{W}{SC_L} \left(1 - \frac{V_\infty^2}{V_c^2}\right) \tag{159}$$

the flight conditions for which maximum heating occurs can be determined since q is proportional to $\rho_\infty^m V_\infty^3$ (where m = 0.8 for turbulent and 0.5 for laminar heating). Therefore, $\dot{q}$ is a maximum when

$$\frac{d\rho_\infty}{dV_\infty} = \frac{-3\rho_\infty}{m V_\infty} \; . \tag{160}$$

From the differentiation of the equilibrium glide Equation (159), however,

$$\frac{d\rho_\infty}{dV_\infty} = \frac{-2\rho_\infty}{V_\infty} \left(1 - \frac{V_\infty^2}{V_c^2}\right)^{-1} \tag{161}$$

When Equations (160) and (161) are combined, the velocity at critical heating may be ascertained.

$$\left(\frac{V_e}{V_c}\right)_{\dot{q}_{max}} = \left(1 - \frac{2m}{3}\right)^{\frac{1}{2}} = \begin{cases} 0.8165 \text{ laminar} \\ 0.6831 \text{ turbulent} \end{cases} \tag{162}$$

or

$$(V_e)_{\dot{q}_{max}} = \begin{cases} 21,170 \text{ laminar} \\ 17,710 \text{ turbulent} \end{cases} \tag{163}$$

Thus the critical heating rates on the vehicle during equilibrium glide re-entry may be determined by substituting Equations (159) and (163) into Equations (153), (156), (157), and (158), assuming $\frac{h_w}{h_s} \ll 1$. Therefore,

$$(\dot{q}_s)_{max} = 8.025 \left(\frac{W}{R_N S C_L}\right)^{0.5}; \text{ laminar} \tag{164}$$

$$(\dot{q}_{LE})_{max} = 5.675 \left(\frac{W \cos^2 \Lambda_e}{R_{LE} S C_L}\right)^{0.5}; \text{ laminar} \tag{165}$$

$$(\dot{q}_{LS})_{max} = 3.131 \left(\frac{W}{x S}\right)^{0.5}; \text{ laminar} \tag{166}$$

$$(\dot{q}_{LS})_{max} = 2.26 \left(\frac{W}{x^{1/4} S}\right)^{0.8}; \text{ turbulent} \tag{167}$$

For thermal equilibrium conditions in which the convective aerodynamic heating is balanced by the surface thermal radiation to space, the temperature may be computed in the following manner:

$$\dot{q} = \epsilon \sigma T^4 \tag{168}$$

Thus

$$\epsilon^{\frac{1}{4}} T_N = 3594 \left(\frac{0.01 W}{S C_L R_N}\right)^{\frac{1}{8}} \tag{169}$$

$$\epsilon^{\frac{1}{4}} T_{LE} = 3297 \left(\frac{0.01 W \cos^2 \Lambda_e}{S C_L R_{LE}}\right)^{\frac{1}{8}} \tag{170}$$

$$\epsilon^{\frac{1}{4}} T_{LS} = 2130 \left(\frac{0.1 W}{x S}\right)^{\frac{1}{8}}; \text{ laminar} \tag{171}$$

$$\epsilon^{\frac{1}{4}} T_{LS} = 2333 \left(\frac{0.1 W}{x^{1/4} S} \right)^{\frac{1}{5}} \qquad \text{turbulent} \qquad (172)$$

Equations (169) and (170) may be used to determine the minimum nose and leading edge radii for specified material temperature limits, sweep angle and glide parameter $(\frac{W}{SC_L})$. Figure 14 is a plot of minimum nose radius versus temperature limit for an $\epsilon = 0.8$.

Equations (171) and (172) may be used to determine the maximum wing loading (W/S) for a given material temperature limit. Figure 15 is a plot of maximum wing loading versus lower surface temperature limit for an ϵ of 0.8, x of 1 foot, and a $C_L = 2 \sin^2 \alpha \cos \alpha$.

II-6. Material Temperature Limits

High temperature materials are required to permit successful re-entry of glide vehicles. The group of materials most applicable for this purpose is entitled "refractory metals." The melting points of some of the most applicable refractory materials are tabulated as follows:

Metal	Melting Point
Tungsten	6170°F
Tantalum	5425°F
Molybdenum	4739°F
Columbium	4380°F

Although the melting temperatures are quite high, these materials all suffer drastically from unsatisfactory oxidation resistance at temperatures in excess of 2000°F. The most desirable method for overcoming the disadvantages of poor oxidation resistance is through alloying. Since little improvement in the oxidation resistance of alloys has been accomplished in the past years, it is generally conceded that coatings are required to protect structural refractory-metal alloys from oxidation. In addition, the bare metals possess low values of emittance; hence, a material coating with high emittance is desired for application to radiation-cooled glide re-entry vehicles. The problem is reduced to one of finding a high emittance coating that can withstand a wide variation in temperature and pressure in an oxidizing atmosphere for prolonged periods. Reference 9 indicates that coatings have been developed with many hours of life at 2500°F and possess a capability at 3000°F for short durations.

Since the nose of the vehicle represents a small portion of the weight yet can contribute a large amount of drag and appreciably affect the maximum L/D, a nose cap should be used with a greater temperature capability than the remainder of the vehicle. The coated carbides, graphites, and various oxides possess high allowable thermal limits (with reduced strength over refractory metals) and represent potential nose cap material. The present "state of the art" thermal capability of nose cap material is in the vicinity of 4000°F.

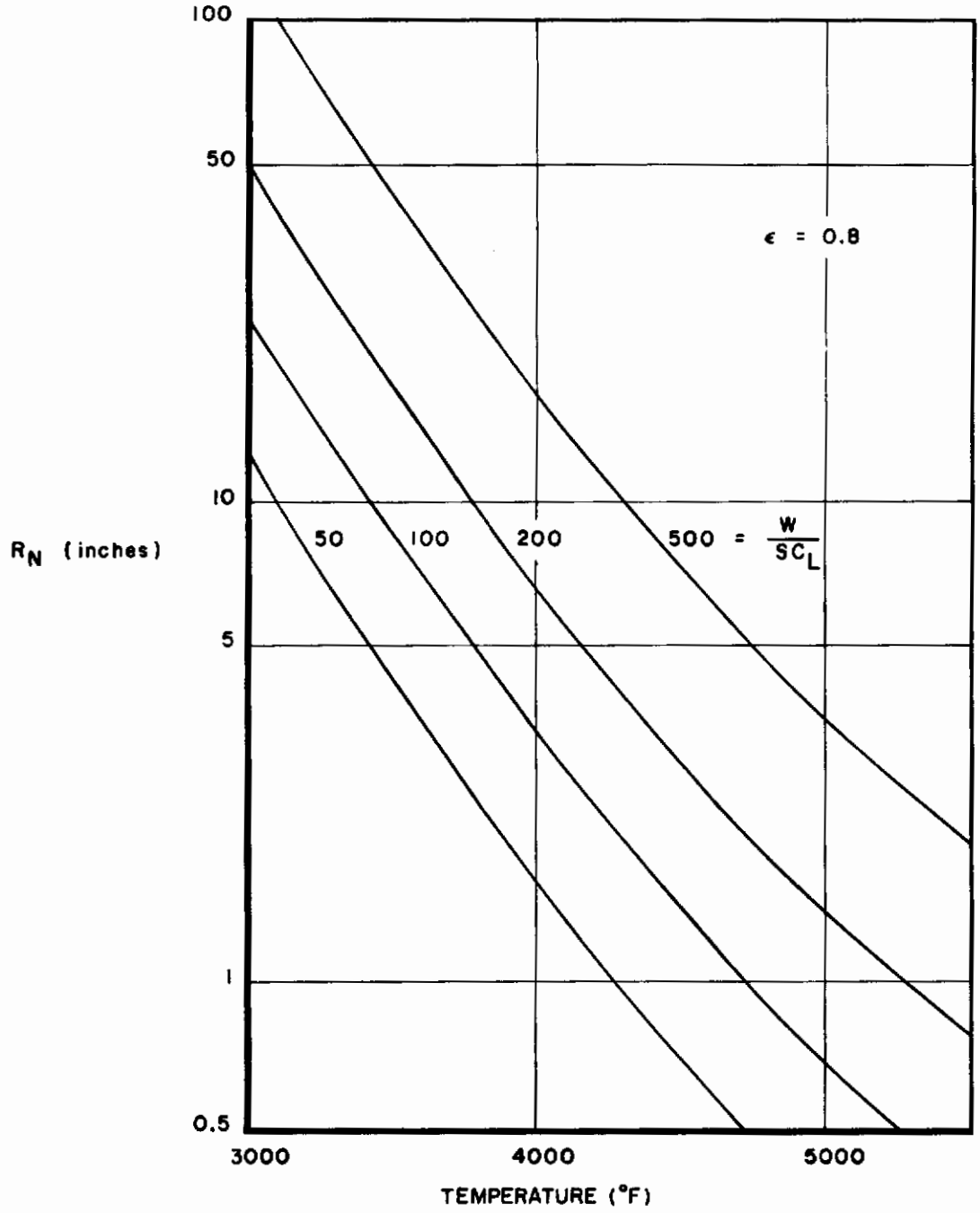

Figure 14. Minimum Radius for Allowable Nose Temperature

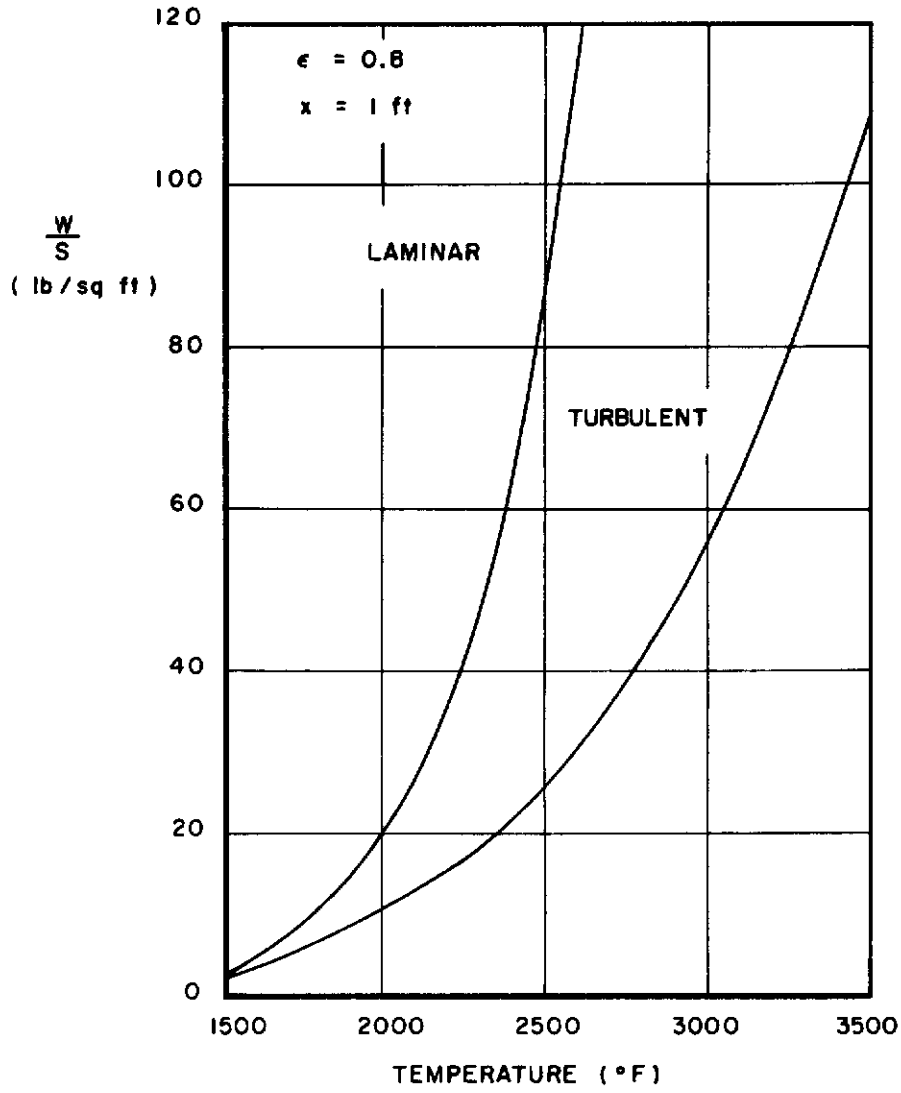

Figure 15. Lower-Surface Critical Temperatures During Glide Re-Entry

APPENDIX III

HYPERSONIC AERODYNAMIC CHARACTERISTICS

III-A. Introduction

There is not available presently an all inclusive compilation of procedures for computing re-entry vehicle force and moment coefficients at hypersonic speeds. Simple techniques are developed in this appendix for rapidly determining the aerodynamic pressures and resultant six-component force and moment characteristics for hypersonic glide vehicles. The methods are applicable between 10° and 30° angle of attack since this covers the $(L/D)_{max}$ range of interest (from 4 to 1). For extremely low or extremely high angles of attack, prediction of the aerodynamic characteristics becomes more complex and need not be investigated here. Techniques herein are further limited to the continuum flow regime in that the aerodynamic characteristics are only of primary interest (for stability and performance) when the dynamic pressure is significant. At low dynamic pressures ($q < 10$ pounds per square foot) reaction controls are required for stability and control of space vehicles. At orbital speed a dynamic pressure of 10 pounds per square foot occurs at an altitude of about 265,000 feet for which the mean free path is about 0.01 foot. The Knudsen number based upon a 10-foot chord would be 10^{-3} indicating that a continuum flow model may be used.

Expressions for the pressure distribution over simple shapes (spheres, cylinders, and planar surfaces) are first derived. A generalized configuration is defined composed of the preceding simple elements, and an analytical expression for the aerodynamic coefficients resulting from integration of the surface pressures is presented. Finally, a summary of the six-component aerodynamic characteristics is tabulated convenient for programming on high speed computers.

III-B. Pressure Distribution Theory

For rapid prediction of aerodynamic forces and pressures on hypersonic aerodynamic vehicles, simple, basic theory is desirable. Perhaps the most popular theory for this type of analysis is Newtonian Impact Theory and its various modifications (References 10 through 19).

The Newtonian flow concept assumes that the free-stream gas, upon striking a surface, loses its component of momentum normal to that surface and then moves along the surface with its tangential component of momentum unchanged (inelastic collision). From this assumption, the pressure coefficient is defined by:

$$C_p = 2 \sin^2 \delta \tag{173}$$

where δ = local flow inclination with the free-stream (angle measured between the velocity vector and the surface) and

$$C_p = \left(\frac{p - p_\infty}{q_\infty} \right)$$

On page 91, Reference 17, the oblique shock relations are modified for the hypersonic case in which the shock wave angle approaches the body slope and the identical result, Equation 173, obtained, which illustrates the basic validity of the Newtonian Flow Theory for hypersonic conditions.

Lees, in Reference 14, presents the Modified Newtonian Theory as:

$$C_p = C_{p_s} \sin^2 \delta \tag{174}$$

where

C_{p_s} = the stagnation pressure coefficient.

A further modification presented by Love in Reference 16 is called the Generalized Newtonian Theory

$$\frac{C_p}{C_{p_{max}}} = \frac{\sin^2 \delta}{\sin^2 \delta_{max}} \quad . \tag{175}$$

This form of the Newtonian theory is useful for pointed shapes such as tangent ogives.

In both of the preceding modifications, the basic form of the equation

$$C_p = k \sin^2 \delta \tag{176}$$

is retained. The k-factor reflects the change in pressure coefficient because of such factors as initial nose slope, Mach number, and change in gas composition, while the $\sin^2\delta$ term accounts for the surface orientation and geometry. Newtonian Flow Theory in its basic form, Equation (173), is applicable only to hypersonic flow over highly inclined surfaces (Reference 19); however, extension of the theory is possible if the form in Equation (176) is retained and the k-factor adjusted. By the use of the theories of known applicability and experimental data, the k-factor for simple geometries is determined herein.

The chief advantage in retaining the expression of the pressure coefficient in the form of Equation (176) is found in the determination of force coefficients in that the required integrations are made relatively simple. A further advantage exists whereby the force coefficient is directly proportional to the k-factor. Therefore, the variation of k-factor over a range of flight conditions directly defines the variation of the force coefficients.

III-B-1. Blunt Surfaces In Impact Flow

Variation of the k-factor for the stagnation region of a surface is illustrated in Figure 16. In this figure, the variation of k for a real gas as computed by Feldman, Reference 20, is shown for a range of Mach numbers and altitudes. Also shown is the variation of k for an ideal gas, as defined in Reference 21 and determined from the following relationship:

$$C_{p_s} = \left(\frac{P_{t_2}}{P_{t_1}} - \frac{P_1}{P_{t_1}} \right) \left(\frac{q}{P_t} \right)_1^{-1} \quad . \tag{177}$$

For a given type of flow and a given Mach number, Figure 16 can be used to determine the C_{p_s} of Modified Newtonian Theory. Note that real gas k-factor values are seen to be rather insensitive to altitude in the range chosen.

The applicability of Modified Newtonian Theory on hemispheres and hemicylinders is illustrated in Figure 17. This figure illustrates that Equation (176), where k is determined from Figure 16, is adequate for evaluating pressures and forces on these suffaces.

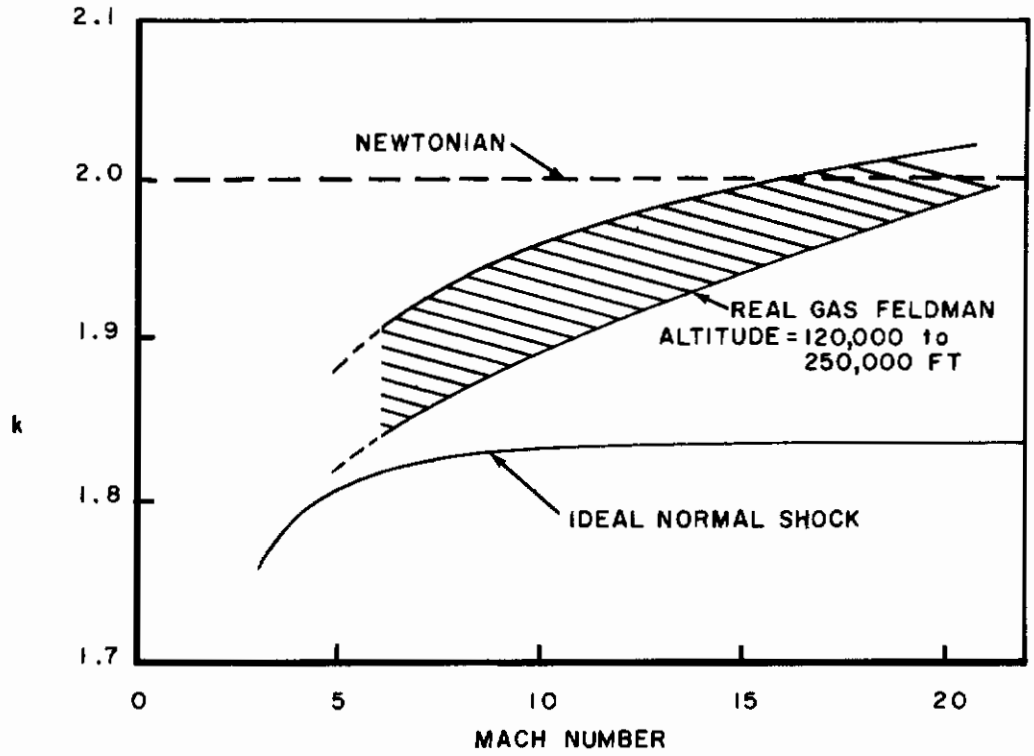

Figure 16. Variation of Stagnation Pressure Coefficient with Mach Number

In the analyzation of swept leading edges, cross-flow theory is used. This reduces the complex three-dimensional problem to a simpler one in two dimensions. Using cross-flow theory Equation (176) becomes

$$C_{p_s} = k \cos^2 \Lambda_e \tag{178}$$

where Λ_e is the effective sweep angle of the leading edge, see Equation (196).

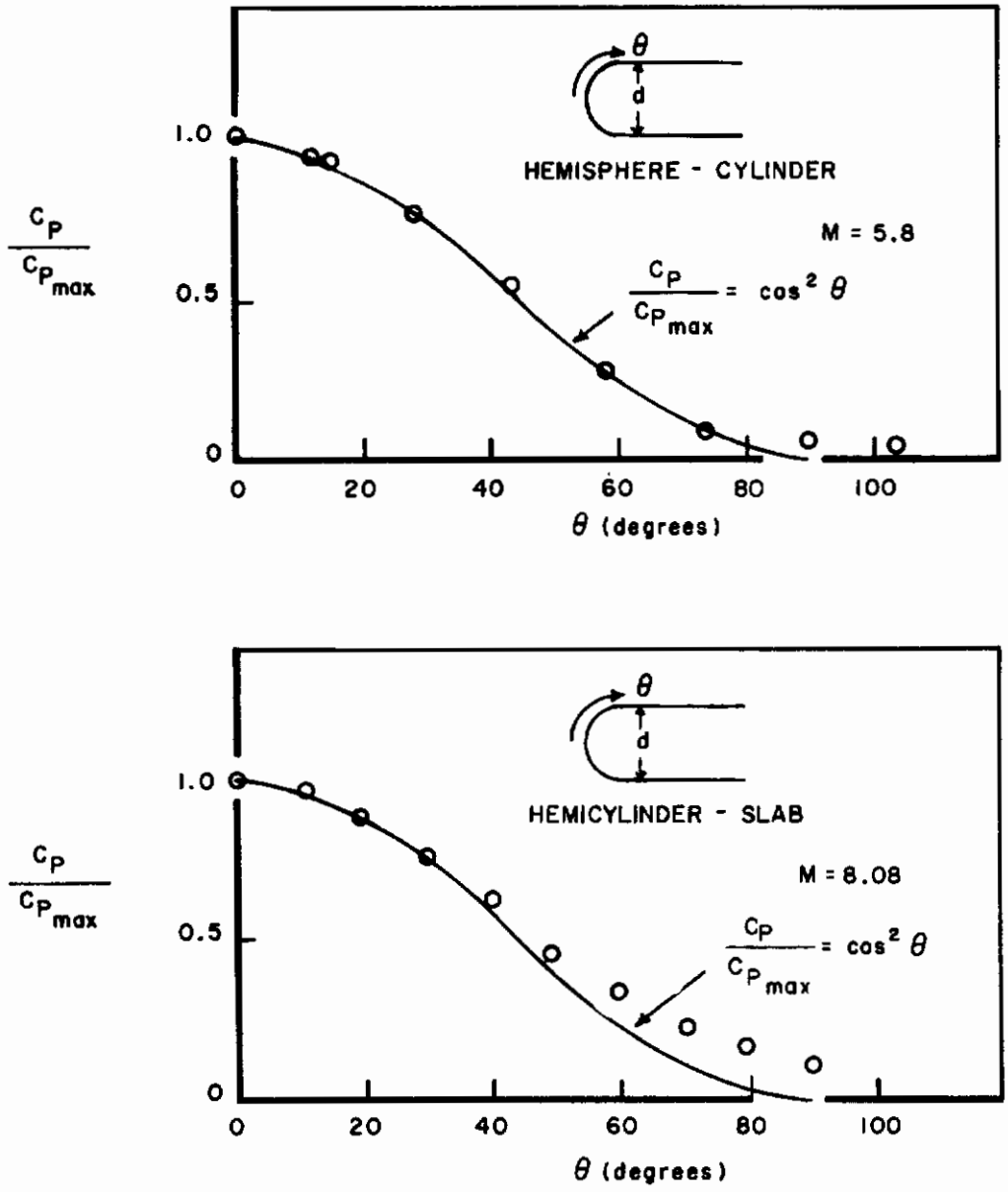

Figure 17. Applicability of Newtonian Theory to Hemispheres and Hemicylinders

III-B-2. Flat Surfaces In Impact Flow

Where the Modified Newtonian Theory is significantly in error, and the surface under consideration is large, some correction must be applied. An example of such a situation is the large lower surface of a blunt swept delta wing. Figure 18 shows the change in pressure coefficients on a blunt wedge due to change in angle of attack (Reference 22). For angles of attack between 5° and 15°, the "tangent wedge" theory appears representative of the mean of the data. For angles of attack above 15°, the flow appears to change in nature and approaches Newtonian values until at 90° the flow stagnates at C_{p_s}.

As no single simple theory would predict the change in the nature of the flow across the angle-of-attack spectrum, several empirical correlation schemes were attempted. The most successful of the schemes considered is the one shown in Figure 19. The faired straight line through the data has the equation

$$k = 1.95 + 0.21 \cot \delta \ . \tag{179}$$

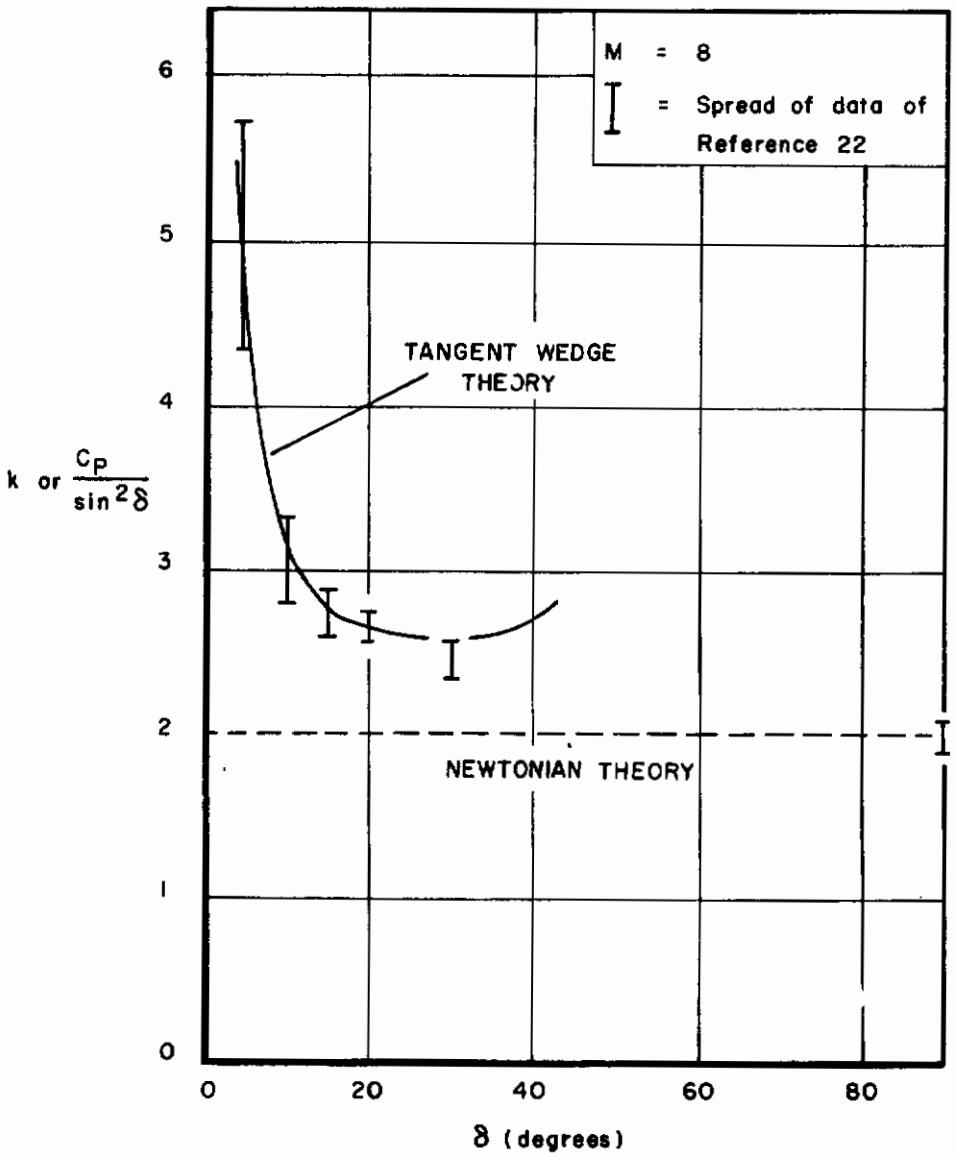

Figure 18. Lower-Surface Pressure Coefficients

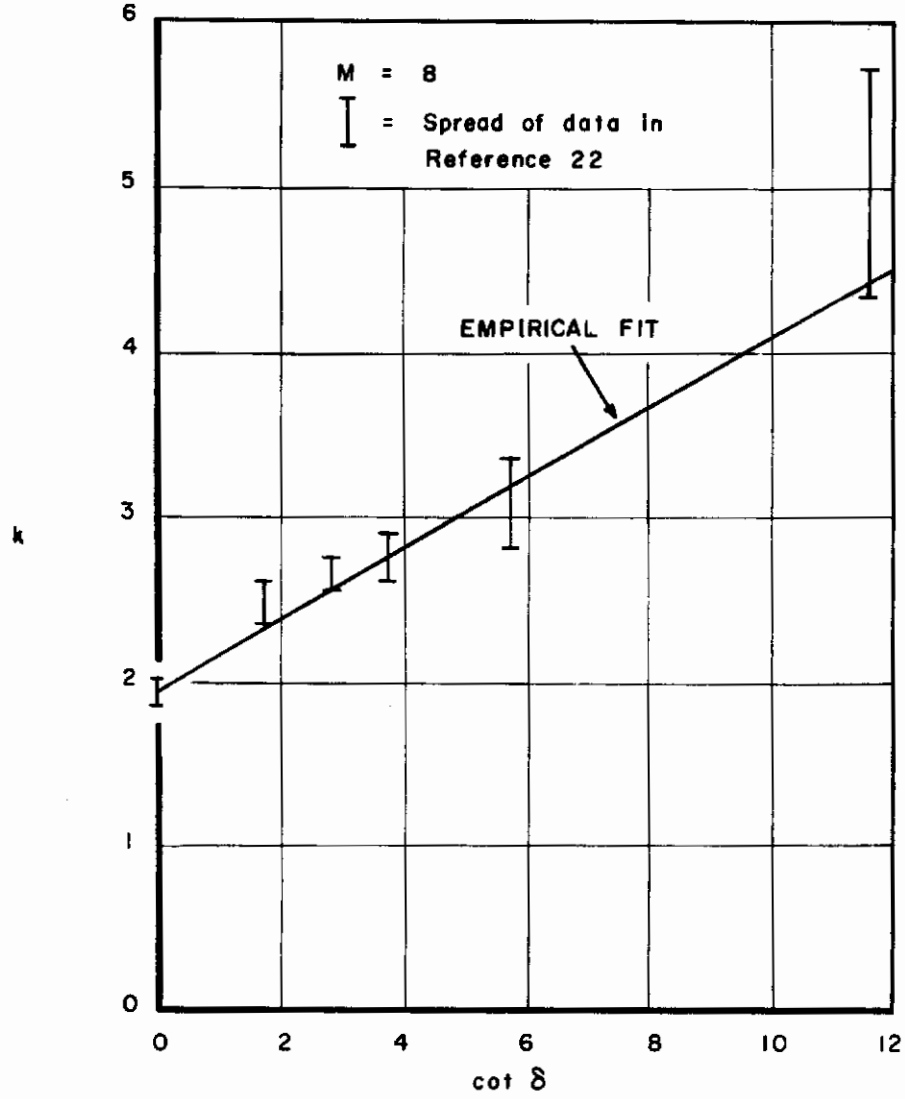

Figure 19. Empirical Correlation of Lower-Surface Pressure Coefficients

For surface inclinations below 10°, the representation in Figures 18 and 19 rapidly loses significance because at $\delta = 0$ for any Mach number, k approaches ∞, which requires a change in the expression for C_p. Interaction and induced pressure effects also become dominant at low angles of attack, which require a change in the analytical procedure. For these reasons, values of α much below 10° will not be considered.

More comprehensive analyses must be applied only when the vehicle in question is considered to fly at low angles of attack. As presently anticipated, only gliders with L/D greater than 4 will fly at angles of attack less than 10°. These vehicles will require refined analysis at low angles of attack.

III-B-3. Induced Pressures

A blunted wedge at angle of attack produces a curved shock wave near the leading edge. Farther away from the leading edge, the shock wave asymptotically approaches that of a sharp wedge. Because of this shock curvature, induced pressures commence at the leading edge shoulder and diminish as the shock curvature reduces (References 23 and 24). Techniques are available (e.g. Belotserkowski, Vaglio-Laurin, etc.) that provide numerical solutions of the flow field from which pressure distributions may be ascertained. However, since numerical results are not yet available in quantity, empirical correlation of the induced pressures was attempted.

From experimental pressure distributions, we determined that a linear variation in ΔC_p from zero at the centerline to $\Delta C_{p_{sh}}$ at the shoulder would adequately account for induced pressure distribution effects on delta wings with relatively small leading-edge radii. From the leading-edge pressure distribution of Reference 22, we observed that the shoulder pressure may be ascertained by shifting the flow angle for the Newtonian pressure coefficient by a small value, ϵ, so that

$$C_{p_{sh}} = k \sin^2 (\alpha + \epsilon) . \tag{180}$$

The induced pressure coefficients at the leading edge shoulder are presented in Figure 20 for various α values. From this figure, it is apparent that the form of Equation (180) adequately accounts for induced pressure if a value of ϵ of 14° is included while the unmodified Newtonian ($\epsilon = 0$) is quite inadequate. For swept leading edges

$$C_{p_{sh}} = k \cos^2 \Lambda_e \sin^2 (\alpha_e + \epsilon) \tag{181}$$

where Λ_e and α_e are defined by Equations (202) and (203). When the identity is used,

$$\cos^2 \Lambda_e \sin^2 \alpha_e = \sin^2 \alpha \cos^2 \beta . \tag{182}$$

Equation (181) may be expanded for small values of β and ϵ as follows:

$$C_{p_{sh}} = k \sin^2 \alpha (1 + 2\epsilon \cot \alpha_e) . \tag{183}$$

The difference in shoulder pressure values is required in the determination of the rolling moment due to yaw of delta wings. This pressure difference can be obtained by using Equation (183) for the right and left shoulders as follows:

$$\underset{R-L}{\Delta} C_{p_{sh}} = 2k\epsilon \sin^2 \alpha (\cot \alpha_{e_R} - \cot \alpha_{e_L}) . \tag{184}$$

For the geometry of interest in this study, we determined from Equation (203) that

$$\underset{R-L}{\Delta} \cot \alpha_e \approx 4\beta .$$

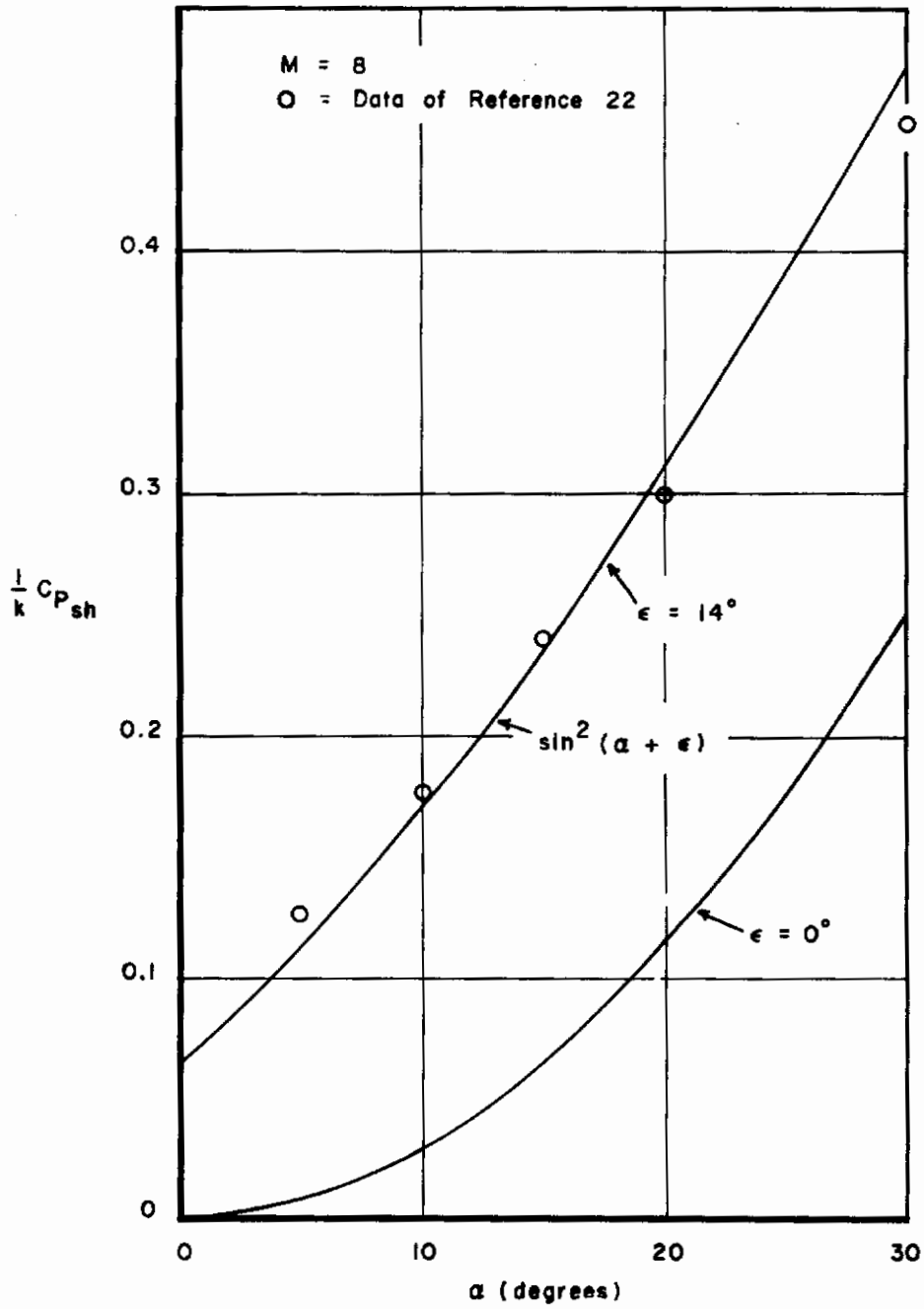

Figure 20. Induced Pressure Correlation of Blunt Leading Edges

Therefore,

$$\underset{R-L}{\Delta} C_{p_{sh}} = k_i \beta \sin^2 \alpha \qquad (185)$$

where

$$k_l = 8k\epsilon = 3.8 \text{ per radian,} \tag{186}$$

III-B-4. Surface Skin Friction

Several methods have been presented in the literature for the prediction of laminar skin friction on flat plates in supersonic and hypersonic flow. These methods are usually complex and laborious to apply and often require evaluation of the flow field behind the compression shock wave. One of the more successful methods is the Reference Enthalpy Method as defined in Reference 6. J.F. Schmidt, in Reference 7, has used this method to predict skin friction over a flat plate for a wide range of flight conditions. Since the data are given in terms of flight parameters instead of flow parameters at the edge of the boundary layer, this reference is ideal. For further simplification of the prediction of laminar skin friction, an empirical curve was fitted to the data presented by Schmidt. This single line is represented by the equation

$$C_{f_{lam}} \sqrt{R_{e_\infty}} = 0.45 \cos\alpha + 4.65 \frac{V_\infty}{10,000} \sin\alpha \cos^{2.2}\alpha \tag{187}$$

where α is the surface angle of attack and

$$C_f = \frac{\tau_w}{\frac{1}{2}\rho_\infty V_\infty^2} \; ; \quad \tau_w = \text{local shear stress.} \tag{188}$$

This equation deviates no more than 20 percent from the data presented by Schmidt for low-altitude high-angle-of-attack flight and is more accurate (approximately by ±10 percent) for the rest of the altitude and angle-of-attack range. This accuracy is sufficient for preliminary design as long as the vehicle is in continuum flow where shear stresses do not dominate. A comparison of the preceding equation with the method of Schmidt is shown in Figure 21. This equation is seen to be applicable for the majority of the re-entry flight corridor.

As is the case with laminar skin friction, many techniques are defined in the open literature for the prediction of turbulent skin friction on flat plates in supersonic and hypersonic flows. Unfortunately, these methods are even more complex than those for laminar flow and rely on empirical relations derived from wind-tunnel or flight-test data. Analysis is often further complicated by the need to evaluate the flow field properties outside the boundary layer. Schmidt, in Reference 8, has used the reference-enthalpy technique to construct a comprehensive series of graphs for the prediction of turbulent skin friction on a flat plate for a wide range of flight parameters. As in the laminar study by Schmidt, the data are given in terms of flight parameters, not local flow parameters, and are, therefore, quite useful in preliminary design. An empirical curve fit of Schmidt's data resulted in the following equation:

$$C_{f_{turb}} (R_{e_\infty})^{0.2} = 0.048 (\sin 4.5\alpha) + 0.70 \frac{V_\infty}{10,000} \cos^{2.25}\alpha \sin^{1.5}\alpha \tag{189}$$

The degree to which this equation covers the analysis of Schmidt is seen in Figure 22. This close comparison proves the equation sufficiently accurate for preliminary design purposes.

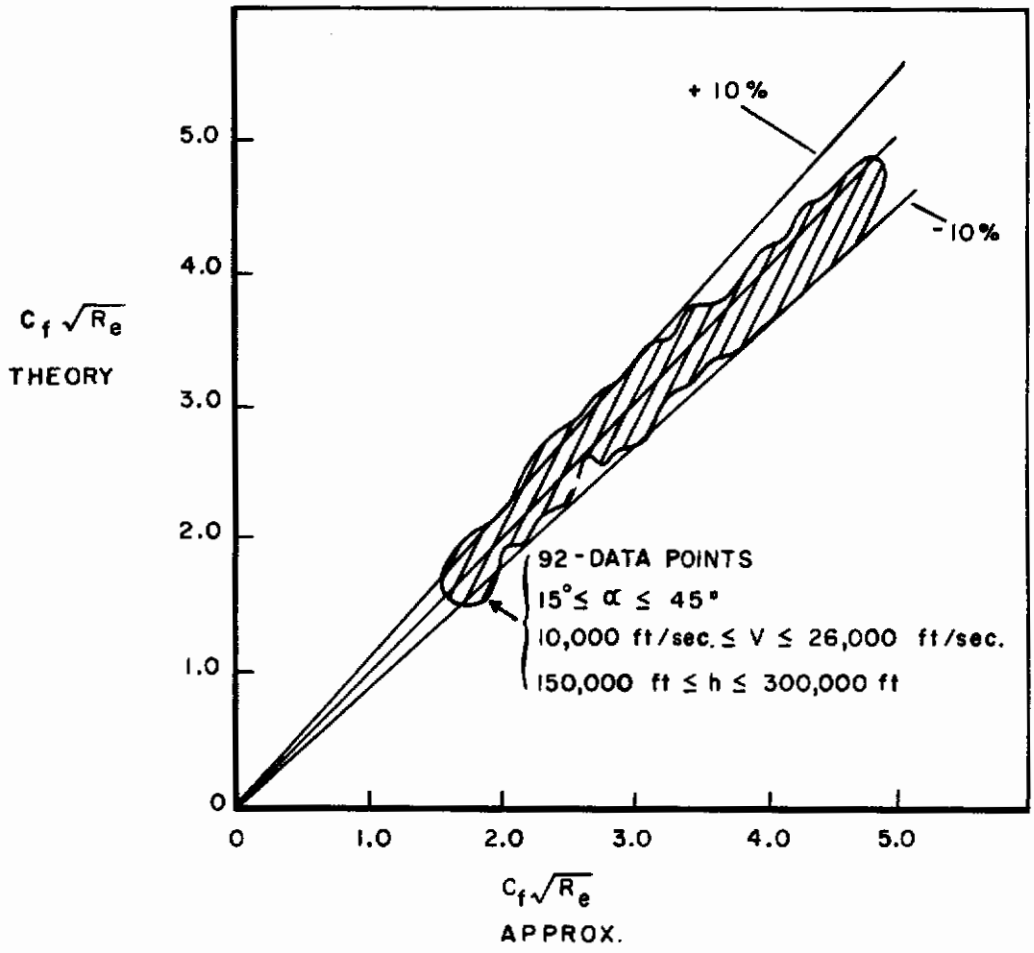

Figure 21. The Comparison of the Empirically Determined Laminar-Skin Friction Equations

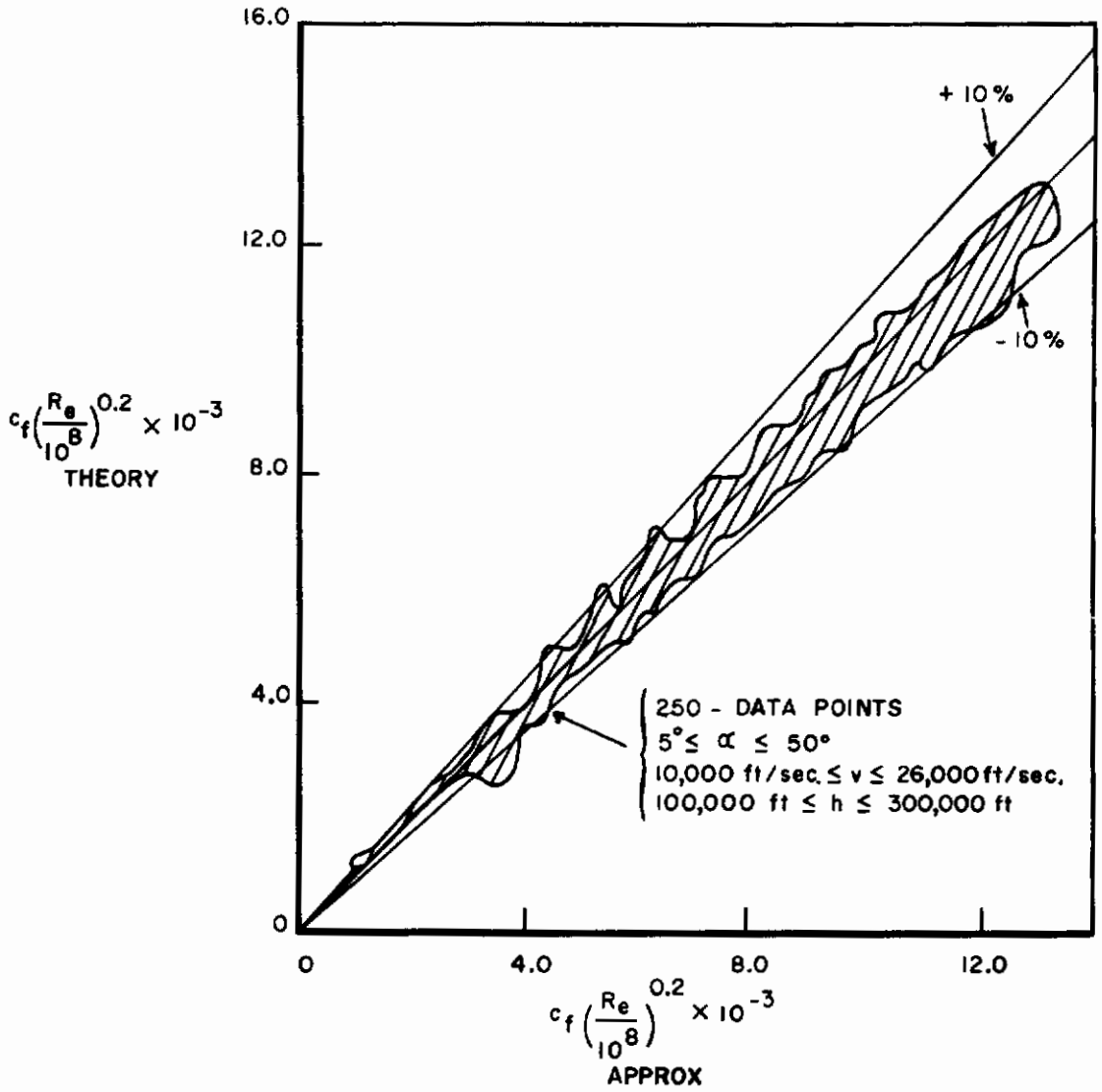

Figure 22. The Comparison of the Empirically Determined Turbulent-Skin Friction Equations

III-C. Determination of Aerodynamic Characteristics

The purpose of this section is to apply the previously developed theoretical and empirical relations to the various basic components of a generalized hypersonic lifting re-entry vehicle and, considering the relative location of the components, describe the aerodynamic characteristics of the configuration. Dependence of the aerodynamic characteristics on surface geometry and orientation is reflected in the Newtonian format

$$C_p = k \sin^2 \delta \tag{176}$$

as developed in the previous section. Determination of δ and integration of C_p for the required aerodynamic characteristics of surfaces with geometries not easily expressed

analytically often can be done precisely only by numerical methods. This complexity is certainly to be avoided whenever possible. For this reason only simple geometric shapes will be analyzed. Quite accurate analysis of complex geometric shapes can be made by proper selection and combination of the simple shapes covered herein.

As important as the definition of the components is their location relative to the center of gravity of the vehicle in question. Therefore, the geometry and the coordinate system of the generalized configuration to be analyzed must be established. Efficient, lifting hypersonic vehicles possess a flat bottom surface with a highly swept planform to maximize C_L and L/D. The nose and leading edges must be blunt (i.e., circular, elliptical, etc.) to withstand the heating environment. Vertical fins are required to provide directional stability and are most practical and effective outboard and in the most rearward position. The body is located on the upper surface unexposed to the high heating. Figure 23 is a three-view sketch of the generalized configuration to be considered showing the general dimensions of the overall configuration, the various components, and the location of the center of gravity.

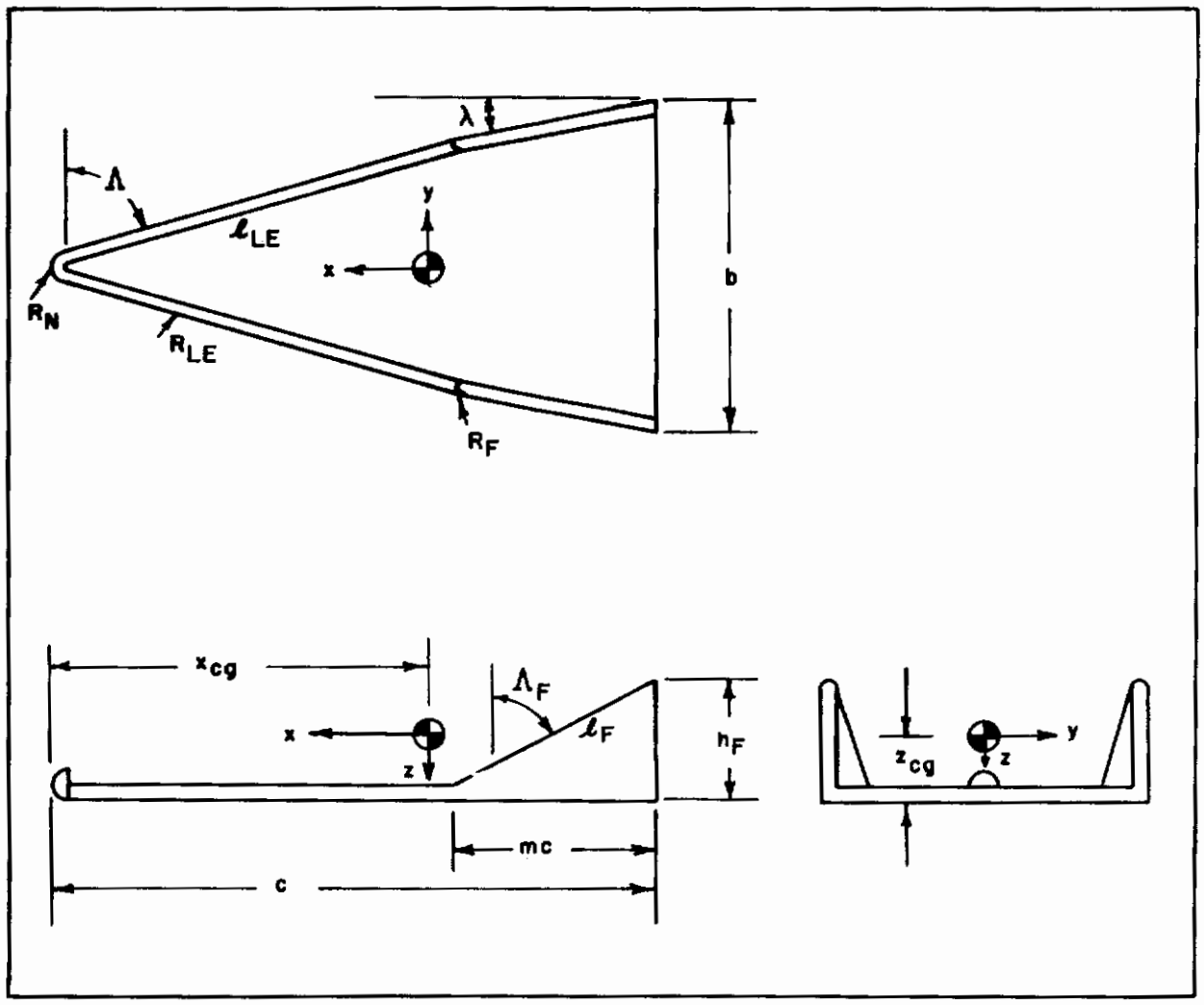

Figure 23. The Generalized Configuration Geometry

With a generalized configuration defined, the aerodynamic characteristics can be analyzed in terms of the general dimensions of the configuration. Defining these general dimensions for a specific configuration permits rapid determination of the aerodynamic characteristics of that configuration.

The aerodynamic coefficients derived herein, and the associated sign convention, are defined in the list of symbols. The symbol and sign convention used by the NASA has been used unless otherwise noted.

Derivation of the coefficients for the different components, in general, followed three basic steps:

1. Determination of a simple representative shape

2. Integration of the theoretical pressure coefficients over that simple shape and evaluation of the basic force coefficients

3. Determination of appropriate moment coefficients through consideration of the displacement distances of the component from the vehicle center of gravity.

Six component characteristics were defined for each configuration component. The lengthy details of the integrations required to derive the aerodynamic force coefficients were omitted and only the results presented.

III-D. Summary of Derived Components

III-D-1. General

A summary of all the derived coefficients are tabulated for convenient reference. Only the basic equations are given. The terms such as k-factor, α, Λ_e, α_e, etc. in the equations must be made to apply to the configuration component that is evaluated.

The lateral and directional coefficients were determined to be linear with β for small angles and hence only the derivatives are presented. Numerical values of the derivatives are in radian measure.

III-D-2. Nose Equations

$$C_N = \frac{\pi R_N^2 k_N}{4S} \sin\alpha \ (1 + \cos\alpha) \tag{190}$$

$$C_A = \frac{\pi R_N^2 k_N}{4S} \frac{(1+\cos\alpha)^2}{2} \tag{191}$$

$$C_m = C_N \frac{x_N}{\bar{c}} - C_A \frac{z_N}{\bar{c}} \tag{192}$$

$$C_{Y_\beta} = -\frac{C_A}{\cos\alpha} \tag{193}$$

$$C_{\ell_\beta} = \frac{C_A}{\cos\alpha} \frac{z_N}{b} \tag{194}$$

$$C_{n_\beta} = -\frac{C_A}{\cos\alpha} \frac{x_N}{b} \tag{195}$$

All derivatives and all angles are in radians.

III-D-3. Leading Edge Equations

These equations are for a pair of leading edge elements.

$$C_N = \left(\frac{4R_{LE}\,\ell_{LE}}{3S}\right) k_{LE} \sin\alpha \,(\cos\Lambda_e + \cos\Lambda \cos\alpha) \tag{196}$$

$$C_A = \left(\frac{4R_{LE}\,\ell_{LE}}{3S}\right) \frac{k_{LE}}{2} \cos\Lambda \,(\cos\Lambda_e + \cos\Lambda \cos\alpha)^2 \tag{197}$$

$$C_m = C_N \frac{x_{LE}}{\bar{c}} - C_A \frac{z_{LE}}{\bar{c}} \tag{198}$$

$$C_{Y_\beta} = -\left(\frac{4R_{LE}\,\ell_{LE}}{3S}\right) k_{LE} \sin^2\Lambda \cos\Lambda_e \,(1+\cos\alpha_e)^2 \tag{199}$$

$$C_{\ell_\beta} = \left(\frac{4R_{LE}\,\ell_{LE}}{3S}\right) k_{LE} \sin\Lambda \,(1+\cos\alpha_e)\left[\frac{z_{LE}}{b} \sin\Lambda \cos\Lambda_e \,(1+\cos\alpha_e) - \frac{y_{LE}}{b}\sin\alpha\right] \tag{200}$$

$$C_{n_\beta} = \left(\frac{4R_{LE}\,\ell_{LE}}{3S}\right) k_{LE} \sin\Lambda \cos\Lambda_e (1+\cos\alpha_e)^2 \left(\frac{-x_{LE}}{b} \sin\Lambda + \frac{y_{LE}}{b}\cos\Lambda\right) \tag{201}$$

$$(\sin\Lambda_e)_{\substack{R\\L}} = \sin\Lambda \cos\alpha \cos\beta \mp \cos\Lambda \sin\beta \tag{202}$$

$$(\cot\alpha_e)_{\substack{R\\L}} = \cos\Lambda \cot\alpha \pm \frac{\sin\Lambda}{\sin\alpha} \tan\beta \tag{203}$$

ℓ_{LE} for one leading edge

III-D-4. Lower Surface Equations

$$C_N = k_\alpha \left(\frac{S_L}{S}\right) \sin^2 \alpha \tag{204}$$

$$C_A = G\left(\frac{S_w}{S}\right) \frac{0.45 \cos \alpha + 4.65 \dfrac{V_\infty}{10{,}000}}{\left(\dfrac{V_\infty c}{\nu_\infty}\right)^{0.5}} \sin \alpha \cos^{2.2} \alpha \quad \text{(laminar)} \tag{205}$$

$$C_A = G\left(\frac{S_w}{S}\right) \frac{0.048 \sin (4.5\alpha) + 0.70 \dfrac{V_\infty}{10{,}000}}{\left(\dfrac{V_\infty c}{\nu_\infty}\right)^{0.2}} \cos^{2.25} \alpha \sin^{1.5} \alpha \quad \text{(turbulent)} \tag{206}$$

$$C_m = C_N \frac{x_L}{\bar{c}} - C_A \frac{z_L}{\bar{c}} \tag{207}$$

$$C_{Y_\beta} = - \frac{C_A}{\cos \alpha} \tag{208}$$

$$C_{\ell_\beta} = \frac{C_A}{\cos \alpha} \frac{z_L}{b} - k_i \sin^2 \alpha \left(\frac{S_L}{S}\right) \frac{2y_{LE}}{9b} \; ; \; k_i = 3.8 \tag{209}$$

$$C_{n_\beta} = - \frac{C_A}{\cos \alpha} \frac{x_L}{b} \tag{210}$$

where

$$G = \frac{2}{n(1+n)} \left[\frac{1 - m^{1+n}}{1 - m^2}\right] ;$$

$$n = \begin{cases} 0.5 & \text{laminar} \\ 0.8 & \text{turbulent} \end{cases}$$

m = planform taper ratio.

III-D-5. Vertical Fin Equations*

$$C_N = -\frac{8R_F \ell_F k_{LE}}{3S} \cos^2(\Lambda_F + \alpha) \sin \Lambda_F \tag{211}$$

$$C_A = 2k_F \frac{S_F}{S} (\lambda^3 \cos^2 \alpha) + \frac{8R_F \ell_F k_{LE}}{3S} \cos^2(\Lambda_F + \alpha) \cos \Lambda_F \tag{212}$$

$$C_m = -2k_F \frac{S_F}{S} (\lambda^3 \cos^2 \alpha) \left(\frac{z_F}{\bar{c}}\right) - \frac{8R_F \ell_F k_{LE}}{3S} \cos^2(\Lambda_F + \alpha) \times \left[\frac{x_{F_{LE}}}{\bar{c}} \sin \Lambda_F + \frac{z_{F_{LE}}}{\bar{c}} \cos \Lambda_F \right] \tag{213}$$

$$C_{Y_\beta} = -4k_F \frac{S_F}{S} (\lambda \cos \alpha) \tag{214}$$

$$C_{\ell_\beta} = -4k_F \frac{S_F}{S} (\lambda \cos \alpha) \left(-\frac{z_F}{b}\right) \tag{215}$$

$$C_{n_\beta} = 4k_F \frac{S_F}{S} (\lambda \cos \alpha) \left(-\frac{x_F}{b} + \lambda \frac{y_F}{b}\right) \tag{216}$$

S_F for one fin

ℓ_F for one fin

---

*The equations are for a pair of fins.

III-D-6. Equations for Transfer of Moment Reference Center

$$\Delta C_m = -C_N \frac{\Delta x}{\bar{c}} + C_A \frac{\Delta z}{\bar{c}} \tag{217}$$

$$\Delta C_{\ell_\beta} = C_{Y_\beta} \frac{\Delta z}{b} \tag{218}$$

$$\Delta C_{n_\beta} = -C_{Y_\beta} \frac{\Delta x}{b} \tag{219}$$

III-D-7. Transformation Equations From Body to Wind Axes

$$C_L = C_N \cos \alpha - C_A \sin \alpha \tag{220}$$

$$C_D = C_N \sin \alpha + C_A \cos \alpha \tag{221}$$

APPENDIX IV

STABILITY ANALYSIS

The dynamics of a vehicle must be such that the handling qualities are within the servo-response capabilities of the pilot. The short period modes are those of primary concern. The dynamical equations of motion may be obtained by analyzing the moment about the oscillating vehicle as follows:

$$\underline{T} = \frac{d\,\underline{H}}{dt} \tag{222}$$

where

$$\underline{H} = \underline{\underline{I}} \cdot \underline{\omega} \tag{223}$$

$$\underline{\underline{I}} = \begin{bmatrix} I_x & 0 & 0 \\ 0 & I_y & 0 \\ 0 & 0 & I_z \end{bmatrix} \quad \text{(principal axes)} \tag{224}$$

$$\underline{\omega} = \dot{\phi}\,\underline{i} + \dot{\theta}\,\underline{j} + \dot{\psi}\,\underline{k} \tag{225}$$

$$\frac{d\underline{H}}{dt} = \frac{\delta\,\underline{H}}{\delta t} + \underline{\omega} \times \underline{H} \tag{226}$$

and where $\frac{\delta}{\delta t}$ denotes differentiation of only the scalar terms. Thus, when Equations (222) through (226) are combined,

$$\begin{aligned} \underline{T} = &\left[I_x \ddot{\phi} + (I_z - I_y)\,\dot{\theta}\,\dot{\psi} \right] \underline{i} \\ &+ \left[I_y \ddot{\theta} + (I_x - I_z)\,\psi\,\dot{\phi} \right] \underline{j} \\ &+ \left[\dot{I}_z \ddot{\psi} + (I_y - I_x)\,\dot{\phi}\,\dot{\theta} \right] \underline{k} \,. \end{aligned} \tag{227}$$

For a pure aerodynamic torque with no damping

$$\underline{T} = (q\,S\,b)\,C_\ell\,\underline{i} + (q\,S\,\bar{c})\,C_m\,\underline{j} + (qSb)\,C_n\,\underline{k} \,. \tag{228}$$

The preceding static aerodynamic moments may be linearized as follows:

$$C_\ell = C_{\ell_\beta}\,\Delta\beta \tag{229}$$

$$C_m = C_{m_\alpha}\,\Delta\alpha \tag{230}$$

$$C_n = C_{n_\beta}\,\Delta\beta \,. \tag{231}$$

The aerodynamic damping of vehicles at hypersonic speeds is virtually nonexistent in that the reduced frequency $(\frac{\omega c}{V})$ is small. For example, a wing with a 50-foot root chord oscillating at 1 cycle per second at Mach Number 20 would produce a reduced frequency of about 10^{-2}. Negligible damping occurs for such a condition and the dynamic stability derivatives may be omitted. It now remains to relate α and β to θ, ψ, and ϕ.

The velocity vector defined in terms of the Euler angles for the pitch-yaw-roll rotational sequence (θ - ψ - ϕ) is as follows (Reference 25):

$$\frac{\underline{V}}{|\underline{V}|} = \cos\psi \cos\theta \,\underline{i} + (\sin\phi \sin\theta - \cos\phi \sin\psi \cos\theta)\,\underline{j} + (\cos\phi \sin\theta + \cos\theta \sin\psi \sin\phi)\,\underline{k}. \quad (232)$$

For small angles of ψ and ϕ, which occur as perturbations from a steady level flight condition,

$$\frac{\underline{V}}{|\underline{V}|} \cong \cos\theta \,\underline{i} + (\phi \sin\theta - \psi \cos\theta)\,\underline{j} + \sin\theta \,\underline{k}. \quad (233)$$

The angle of attack is defined as follows:

$$\tan\alpha = \frac{w}{u} = \frac{\underline{V} \cdot \underline{k}}{\underline{V} \cdot \underline{i}} = \frac{\sin\theta}{\cos\theta} = \tan\theta. \quad (234)$$

Thus

$$\alpha = \theta \quad (235)$$

and

$$\ddot{\alpha} = \ddot{\theta} \quad (236)$$

The angle of sideslip, β, measured in the wind reference plane is defined as follows:

$$\sin\beta = \frac{v}{|\underline{V}|} = \frac{\underline{V}}{|\underline{V}|} \cdot \underline{j} = \phi \sin\theta - \psi \cos\theta \quad (237)$$

for small sideslip angles, and since $\theta = \alpha$ (Equation 235),

$$\beta = \phi \sin\alpha - \psi \cos\alpha \quad (238)$$

and

$$\dot{\beta} = \dot{\phi} \sin\alpha - \dot{\psi} \cos\alpha \quad \text{for fixed } \alpha. \quad (239)$$

The longitudinal short-period mode for a hypersonic vehicle may be obtained by setting $\dot{\phi}$ and $\dot{\psi}$ equal to zero in Equations (227), (228), and (230) as follows:

$$I_y \ddot{\theta} = (q S \bar{c} C_{m_\alpha}) \Delta\alpha \quad ; \quad (240)$$

however, $\ddot{\theta} = \ddot{\alpha}$ from Equation (236); therefore

$$\ddot{\alpha} - \left(\frac{q S \bar{c}}{I_y} C_{m_\alpha} \right) \Delta\alpha = 0 , \tag{241}$$

which is the equation for simple harmonic motion in α with angular frequency ω_α.

$$\omega_\alpha^2 = - \left(\frac{q S \bar{c}}{I_y} C_{m_\alpha} \right) \tag{242}$$

The lateral oscillation short period mode (Dutch Roll) may be obtained by setting $\dot{\theta}$ equal to zero in Equations (227), (228), (229), and (230). See Reference 26.

Therefore,

$$I_x \ddot{\phi} = (q Sb C_{\ell_\beta}) \Delta\beta \tag{243}$$

$$I_z \ddot{\psi} = (q Sb C_{n_\beta}) \Delta\beta . \tag{244}$$

Using Equations (243) and (244) to eliminate $\ddot{\phi}$ and $\ddot{\psi}$ from Equation (239) produces

$$\ddot{\beta} = \left(\frac{C_{\ell_\beta}}{I_x} \sin\alpha - \frac{C_{n_\beta}}{I_z} \cos\alpha \right) (q Sb) \Delta\beta , \tag{245}$$

which is the equation for simple harmonic motion in β with angular frequency ω_β.

$$\omega_\beta^2 = q Sb \left(\frac{C_{n_\beta}}{I_z} \cos\alpha - \frac{C_{\ell_\beta}}{I_x} \sin\alpha \right) . \tag{246}$$

Pilot-rated flight-simulator studies have indicated that the most desirable operating conditions are when the short period mode of the vehicle has the following characteristics:

frequency, $f \approx 0.7$ $\begin{cases} > 0.4 \\ < 1.0 \end{cases}$ cycles per second

damping ratio, $\zeta \approx 0.7$ $\begin{cases} > 0.4 \\ < 1.0 \end{cases}$

Oscillations of this type are within man's servo-response characteristics yet the vehicle possesses satisfactory sensitivity to control inputs (neither too sluggish nor too sensitive). Present day aircraft attain these handling qualities either by aerodynamic means or artificially by "adaptive control" features. Hypersonically, negligible aerodynamic damping occurs ($\zeta \rightarrow 0$ for the emergency situation of artificial augmentation inoperative), which necessitates changing the handling quality criteria. Since zero damping implies periodic motion with constant amplitude, the pilot must damp out oscillations by "out-of-phase" control modulation. For accomplishment of this, the oscillation must

be of a long period (P > 10 seconds) to permit sufficient time for pilot phase control. Therefore, with zero damping, near zero frequency is required. This condition is not comfortable to fly but considered acceptable through flight simulator training.

For ω_α and ω_β equal to zero, then from Equations (242) and (243)

$$C_{m_\alpha} = 0 \tag{247}$$

$$C_{n_\beta} = 0 \tag{248}$$

$$C_{\ell_\beta} = 0 . \tag{249}$$

Hence, the preceding three conditions are the hypersonic stability constraints for flight at maximum L/D.

APPENDIX V

LOW SPEED ANALYSIS

The low-speed flying requirements impose several constraints on a hypersonic lifting vehicle. First, the vehicle must be able to execute a satisfactory horizontal landing and, secondly, it must possess acceptable stability. Low-speed performance requirements are not considered important since most of the maneuverability is accomplished at hypersonic speeds, although some low-speed maneuverability is a fall-out from the landing constraint. The point is that the vehicle will not be designed for good low-speed performance but must accept the amount available.

V-A. Landing

The method presently deemed most desirable for landing hypersonic aircraft is the "aiming point" technique used in the X-15. In this method the pilot dives the vehicle at a point on the earth's surface several thousand feet before the runway, then executes a flare at some predetermined altitude to a shallow glide angle, and decelerates by increasing the angle of attack until touchdown at some preselected speed. By the use of this "Dynamic Approach" technique, vehicles of low subsonic L/D may be safely landed. In this maneuver the highest lift coefficient is required at touchdown (Reference 27). For $\dot{\gamma} = 0$

$$(C_L)_{max} = \frac{(\frac{W}{S})}{q_{TD}} \tag{250}$$

The lift coefficient for low aspect ratio (AR) airfoils may be estimated by the theory of Jones (Reference 28)

$$C_L = \frac{\pi}{2} AR \alpha . \tag{251}$$

When the last two equations are combined,

$$\frac{W}{S\,AR} = \frac{\pi}{2} q_{TD} \alpha . \tag{252}$$

For touchdown velocities less than about 200 knots and for angles of attack less than 15°,

$$\frac{W}{S\,AR} \leq 50 \text{ pounds per square foot.} \tag{253}$$

Hence the preceding relationship between wing loading and aspect ratio becomes the landing constraint.

V-B. Low Speed Stability

The low-speed directional stability constraint is used to determine the size of the vertical fin. The yawing moment for two dorsal fins may be expressed as follows:

$$\eta = \left(\frac{dC_L}{d\alpha}\right) \beta \; q\,(2S_F)\,(-x_F) \tag{254}$$

or in coefficient form

$$C_{n_\beta} = \left(\frac{dC_L}{d\alpha}\right)\left(\frac{2S_F}{S}\right)\left(\frac{-x_F}{b}\right) \tag{255}$$

For low aspect ratio fin planform (see Equation 251),

$$\frac{dC_L}{d\alpha} = \frac{\pi}{2} AR_F \; . \tag{256}$$

For the center of gravity near the centroid of the planform (0.65 c) and triangular type fin planforms

$$x_F = -\frac{2}{3}(0.35\,c) \; . \tag{257}$$

Also for delta planforms

$$\frac{c}{b} = \frac{1}{2} \tan \Lambda \tag{258}$$

and

$$AR_F = 2 \cot \Lambda_F \; . \tag{259}$$

Thus by substitution of Equations (256) through (259) into Equation (255)

$$C_{n_\beta} = \frac{0.7\pi}{3}\left(\frac{S_F}{S}\right)\frac{\tan \Lambda}{\tan \Lambda_F} \; . \tag{260}$$

For clipped deltas of taper ratio, m,

$$\frac{S_F}{S} = \frac{m^2 \cot \Lambda_F}{2(1-m^2)\cot \Lambda} \; . \tag{261}$$

Therefore Equation (260) becomes

$$C_{n_\beta} = \frac{1.4\pi}{3}\left(\frac{1-m^2}{m^2}\right)\left(\frac{S_F}{S}\right)^2 . \tag{262}$$

Perkins and Hage (Reference 29) present a formula for the desirable quantity of C_{n_β} for satisfactory handling characteristics.

$$(C_{n_\beta})_{desired} = 0.0005\left(\frac{W}{S\,AR}\right)^{\frac{1}{2}} 57.3/rad \tag{263}$$

When the last two equations are combined, the required fin area may be ascertained

$$\frac{S_F}{S} = 0.14 \left(\frac{m^2}{1-m^2}\right)^{\frac{1}{2}} \left(\frac{W}{S\,AR}\right)^{\frac{1}{2}} . \tag{264}$$

For m = 0.3 (Section 3-C) and $\frac{W}{S\,AR}$ = 50 (Equation 253),

$$\frac{S_F}{S} \approx 0.1 . \tag{265}$$

Thus, the fin area requirement becomes the low speed stability constraint.

LIST OF REFERENCES

1. Forsyth, A.R.; Calculus of Variations; Cambridge University Press, 1927.

2. Lees, Lester; "Laminar Heat Transfer Over Blunt Nosed Bodies at Hypersonic Flight Speeds," Jet Propulsion; Vol 26; April 1956; No. 4, p. 259.

3. Creager, Marcus O.; Effects of Leading-Edge Blunting on the Local Heat Transfer and Pressure Distributions Over Flat Plates in Supersonic Flow; NASA TN 4142, National Aeronautics and Space Administration, 1957.

4. Wagner, Pine, and Henderson; Laminar Heat Transfer and Pressure Distribution Studies on a Series of Re-entry Nose Shapes at a Mach Number of 19.4 in Helium; NASA TN D-891; National Aeronautics and Space Administration, June 1961.

5. Hankey, W.L., Neumann, R.D., Flinn, E.V.; Design Procedures for Computing Aerodynamic Heating at Hypersonic Speeds; WADC TR 59-610, Wright Air Development Center, Wright-Patterson Air Force Base, Ohio, 1960.

6. Eckert, E.R.G.; Survey of Heat Transfer at High Speeds; WADC TR 54-70, Wright Air Development Center, Wright-Patterson Air Force Base, Ohio, 1954.

7. Schmidt, J.F.; Laminar Skin Friction and Heat Transfer Parameters for a Flat Plate at Hypersonic Speeds in Terms of Free-Stream Flow Properties; NASA TN D-8, National Aeronautics and Space Administration, September 1959.

8. Schmidt, J.F.; Turbulent Skin Friction and Heat Transfer Coefficients for an Inclined Flat Plate at High Hypersonic Speeds in Terms of Free-Stream Flow Properties; NASA TN D-869, National Aeronautics and Space Administration, May 1961.

9. Krier, C.A.; Coatings for the Protection of Refractory Metals from Oxidation; DMIC Report 162; Battalle Memorial Institute, Columbus, Ohio, November 1961.

10. Hayes, Wallace D., and Probstein, R.F.; Hypersonic Flow Theory; Academic Press, New York, 1959, Chapter III.

11. Shapiro, Ascher H.; The Dynamics and Thermodynamics of Compressible Fluid Flow; Volumes I and II, The Ronald Press Company, New York, 1953.

12. Grey, Don J.; Drag and Stability Derivatives of Missile Components According to Modified Newtonian Theory; AEDC TN-60-191, November 1960.

13. Grimminger, G., Williams, E.P., and Young, G.B.S.; "Lift on Inclined Bodies of Revolution in Hypersonic Flow;" Journal of Aeronautical Sciences, Volume 17, No. 11, p. 675-690, November 1950.

14. Lees, Lester; "Hypersonic Flow," Proceedings IAS-RAeS Fifth International Aeronautical Conference, Los Angeles, California, June 20-23, 1955.

15. Lees, L.; "Recent Developments in Hypersonic Flow;" Jet Propulsion, p. 1162-1178, November 1957.

LIST OF REFERENCES (CONT'D)

16. Love, E.S.; "Generalized Newtonian Theory," Journal of the Aero/Space Sciences, p. 314, May 1959.

17. Kaufman, Louis G. II, and Scheuing, Richard A.; "An Introduction to Hypersonics," Grumman Aircraft Engineering Corporation Report, RE-82, October 1956.

18. Truitt, Robert W.; Hypersonic Aerodynamics; The Ronald Press Company, New York, 1959.

19. Malvestuto, Frank S., Jr., et al; Study to Determine Aerodynamic Characteristics on Hypersonic Re-Entry Configurations; WADD Technical Report 61-56, Part II, Volume I, Wright Air Development Division, Wright-Patterson Air Force Base, Ohio, August 1962.

20. Feldman, Saul; Hypersonic Gas Dynamic Charts for Equilibrium Air; AVCO Research Lab., AVCO Manufacturing Corporation, January 1957.

21. Equations, Tables, and Charts for Compressible Flow; NASA Report 1135, National Aeronautics and Space Administration, 1953.

22. Martellucci, A., and Fields, A.; Pressure Distribution on Blunted Flat Plates with Surface Inclination; General Applied Science Laboratories Data Report No. 5134-5, Technical Report No. 171, June 1960.

23. Creager, M.O.; Effects of Leading-Edge Blunting on the Local Heat Transfer and Pressure Distributions Over Flat Plates in Supersonic Flow; NASA TN 4142, National Aeronautics and Space Administration, December 1957.

24. Creager, M.O.; The Effect of Leading-Edge Sweep and Surface Inclination on the Hypersonic Flow Field Over a Blunt Flat Plate; NASA Memo 12-25-58A, National Aeronautics and Space Administration, January 1959.

25. Brown, R.C., et al; Six-Degree of Freedom Flight Path Study Generalized Computer Program, Part I, Problem Formulation; WADD TR 60-781, Wright Air Development Division, Wright-Patterson Air Force Base, Ohio, November 1960.

26. Etkin, Bernard; Dynamics of Flight, John Wiley & Sons, Inc., New York, 1959.

27. Matranga, Gene J.; Analysis of X-15 Landing Approach and Flare Characteristics Determined from the First 30 Flights, NASA TN D-1057, National Aeronautics and Space Administration, 1961.

28. Donovan, A.F. (Editor); Aerodynamic Components of Aircraft at High Speeds Volume VII (High Speed Aerodynamics and Jet Propulsion); Princeton University Press, N. J., 1957.

29. Perkins, C.D., and Hage, R.E.; Airplane Performance Stability and Control, John Wiley & Sons, Inc., New York, 1949.